REPORT DOCUMENTATION PAGE

AFRL-SR-AR-TR-06-0138

1. REPORT DATE *(DD-MM-YYYY)*	2. REPORT TYPE	3. DATES COVERED *(From - To)*
15-04-2006	Final Technical Report	August 2005 - April 2006

4. TITLE AND SUBTITLE	5a. CONTRACT NUMBER
Electromagnetic Launching For Affordable Agile Access to Space Appendix: Estimate Electromagnetic Launch	FA9550-05-C-0108
	5b. GRANT NUMBER
	5c. PROGRAM ELEMENT NUMBER

6. AUTHOR(S)	5d. PROJECT NUMBER
Meinke, Rainer, Dr. Guiterrez, Hector, Dr. Kirk, Daniel, Dr.	5e. TASK NUMBER
	5f. WORK UNIT NUMBER

7. PERFORMING ORGANIZATION NAME(S) AND ADDRESS(ES)	8. PERFORMING ORGANIZATION REPORT NUMBER
Advanced Magnet Laboratory Inc. 328-A West Hibiscus Blvd. Melbourne, Fl 32901	

9. SPONSORING/MONITORING AGENCY NAME(S) AND ADDRESS(ES)	10. SPONSOR/MONITOR'S ACRONYM(S)
Air Force Office of Scientific Research/~~PKC~~ *NA* 875 North Randolph Street Suite 325, Room 3112 Arlington, VA 22203 *Dr. Mitat A. Birkan*	
	11. SPONSOR/MONITOR'S REPORT NUMBER(S)

12. DISTRIBUTION/AVAILABILITY STATEMENT

Approved for public release; distribution unlimited *Distribution A*

13. SUPPLEMENTARY NOTES

14. ABSTRACT

The conceptual design of a novel, hypersonic electromagnetic launch system has been developed, which offers reliable, r access to space. While the concept can be scaled in both mass and launch speed, the performed study assumes a 100-l leaving the launcher at 7,000 m/sec. The projectile is propelled and levitated by electromagnetic forces inside a tube filled pressure helium. A controlled acceleration profile, fully adjustable to the requirements of various missions, is used to reach in a 500-meter long launch tube. A constant-flux synchronous motor concept, developed under this contract, is a breakth technology that provides contact-free propulsion and self-centering suspension with sufficient stiffness and thrust. Rapid s introduced into the projectile prior to acceleration enhances its trajectory stabilization. The use of high-current, persistent superconducting coils in the projectile generates high thrust force with near-zero heat dissipation. No brushes or projectile supplies are needed, eliminating contact phenomena. The low-pressure helium atmosphere in the launcher reduces aero

15. SUBJECT TERMS

Electromagnetic launch, hypersonic, constant-flux synchronous motor, magnetic levitation, contact-free, self centering, spinning projectile, persistent mode, superconducting coils, low pressure helium, scalable, direct LEO insertion, kinetic kill weapon

16. SECURITY CLASSIFICATION OF:			17. LIMITATION OF ABSTRACT	18. NUMBER OF PAGES	19a. NAME OF RESPONSIBLE PERSON
a. REPORT	b. ABSTRACT	c. THIS PAGE	UU	48	Dr. Rainer Meinke
U	U	U			19b. TELEPHONE NUMBER *(Include area code)* 321-728-7543

Standard Form 298 (Rev. 8/98)
Prescribed by ANSI Std. Z39.18
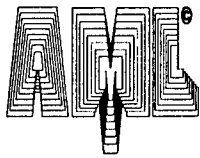
Air Force STTR - Final Report

Electromagnetic Launching
For
Affordable Agile Access to Space

Rainer B. Meinke, Ph.D

Advanced Magnet Laboratory
Melbourne, FL 32901

Hector Guiterrez, Ph.D. and Daniel R. Kirk, Ph.D.

Department of Mechanical and Aerospace Engineering
Melbourne, FL 32901

Executive Summary.

The conceptual design of a novel electromagnetic launch system has been developed. While the concept can be scaled in both mass and launch speed, the performed study assumes a 100-kg projectile leaving the launcher at 7,000 m/sec. The projectile is propelled and levitated by electromagnetic forces inside of a low pressure tube filled with helium at about 10 torr. A fully controlled acceleration profile, which can be adjusted to meet the requirements of various missions, is used to reach 5000 gee in a 500-meter long launch tube.

With an individual launch cycle of approx. 0.5 sec, several launches per hour are possible depending on the type of energy storage system. Depending on range and altitude of the desired mission, the launch tube should be inclined to angles between 25 and 60 degrees. To achieve the desired launch angle with a support structure easy to implement, the launch tube can be partially built underground. The system is powerful enough to reach low earth orbit, but could also be scaled to launch projectiles over distances of a few hundred miles in kinetic kill applications. The proposed technology is highly reliable and responsive: preparation for launch (the time needed to load the projectile into the launch tube, cool the superconducting coils on the projectile and charge up the energy storage system for launch) should be in the order of a few hours (pre-cooling the superconducting projectiles would significantly increase responsiveness by enabling launch within less than one hour). The system's reliability and survivability is expected to be very high, since the projectile has no mechanical contact with the launch track during the acceleration cycle, and the heat dissipation during launch is minimal.

The breakthrough concept of the proposed system is the invention of a pulsed synchronous motor that generates a constant magnetic flux zone moving with the projectile in a traveling wave. Thrust and levitation is provided by current pulses supplied to the track coils adjusted in time (leading and trailing edge, pulse duration and pulse frequency) so that no magnetic flux change is seen by the projectile coils during launch. The cylindrical projectile is equipped with superconducting coils operated in persistent mode, charged prior to launch. Constant flux translates to no voltage or additional currents being induced, which prevents the projectile coils from quenching or overheating. The projectile coils, built in a cable-in-conduit assembly as in pulsed fusion magnets, can carry persistent currents of up to 50 kA under severe operating conditions in pulsed magnetic fields with no need for induction or external power supply. The proposed constant flux synchronous motor (CFSM) is self-centering and avoids mechanical contact between the track and the projectile - the electromagnetic forces and torques are sufficient to compensate for the aerodynamic disturbance forces and moments during launch. The projectile's trajectory is further stabilized by inducing spinning motion prior to launch.

A low pressure helium atmosphere inside of the launch tube is proposed, which nearly eliminates both aerodynamic and heat transfer effects (forces, torques and heating) due to high speed gas flow around the projectile, with large safety margins. The proposed technology therefore removes several of the technical problems that have made hypersonic electromagnetic launch unfeasible, in particular the inductive heating of the projectile when a contact-free armature is desired.

Injection to the atmosphere at ground level at hypersonic speeds creates the need of a careful study of ablation and heat management in the projectile. Our preliminary analysis and

2

existing studies indicate the feasibility of the proposed mission; however, further studies are needed to fully qualify ground-level launching.

During the proposed Phase-2 of this project, the key components of the system will be qualified. This includes the operation of the Constant-Flux-Synchronous Motor (CSFM), the superconductor for the projectile coils and the ablation and thermal management of the projectile during atmospheric coasting. The feasibility and efficiency of the CFSM concept will be experimentally demonstrated on a linear test rig. The required superconducting coils will be developed and tested for mechanical and quench reliability under simulated operational conditions. Ablation and heat dissipation in the projectile will be tested using a high-intensity electron beam that mimics the heat density induced by atmospheric coasting - although not all aspects of the aerodynamic erosion and heating during atmospheric flight can be simulated, important insight will be gained.

The proposed electromagnetic launch system, based on the constant-flux synchronous motor concept, is a breakthrough technology that eliminates several of the inherent limiting factors of conventional electromagnetic launchers. The main advantages of this concept are:

- The CFSM principle provides contact-free propulsion and self-centering suspension forces with sufficient stiffness and thrust force.

- No brushes or projectile power supplies are needed, eliminating complex contact phenomena at high speeds, its inherent limitation of power rate, and undesirable arcing effects at the end of the launcher.

- The use of high-current, persistent-mode superconducting coils in the projectile generate high thrust force with near-zero heat dissipation.

- The traveling-wave constant-flux concept provides the required thrust with near-zero heat dissipation in the projectile. This eliminates the inherent speed limitation of induction-based launchers.

- Heat dissipation in the launcher is minimal and distributed, resulting in higher reliability and survivability of the launch tube.

- Low-pressure helium atmosphere in launcher reduces aerodynamic disturbances and aerothermal heating during launch to negligible levels.

- Projectile stabilization is aided by spinning in a low-pressure environment during launch. This contributes to improved range and accuracy.

- The proposed concept can be used in a wide range of applications from kinetic kill weapons to direct LEO insertion of small payloads.

- The proposed concept is highly scalable to various payload sizes and launch speeds.

- The acceleration profile can be adjusted according to mission requirements.

For these reasons, the proposed Phase 2 project constitutes a major step towards the realization of reliable, responsive, high-performance hypersonic electromagnetic launch systems.

3

1. Introduction

Electromagnetic (EM) launching has been pursued in the last three decades as an efficient and economical alternative to chemical propulsion for military and aerospace applications. Although several different concepts have been proposed, a number of unresolved technical challenges have prevented it from becoming a reality. Broadly speaking, the critical limitations of EM launching have been (i) large heat dissipation, leading to potential damage to both payload and launcher when reaching high speeds, (ii) complex wear and contact phenomena resulting from mechanical contact at high speeds, (iii) the lack of an efficient method to generate current in the projectile without excessive heating of the payload.

This paper presents the constant-flux synchronous motor (CFSM), a novel concept that addresses most of these critical problems. The CFSM launcher is based on a constant magnetic flux zone that moves with the projectile in a traveling wave. Constant-flux operation eliminates inductive heating of the projectile. Superconducting rings operating in persistent mode are used as current source in the projectile, eliminating the need of feeding the launch vehicle through brushes, contact armatures or AC induction. The resulting contact-free, self centering suspension and propulsion dramatically improves survivability (wear and tear) of the launcher since heat dissipation in the track during launch is relatively small and distributed over the length of the launcher. A conical/cylindrical projectile design allows stabilization by spinning, introduced at the home position prior to launch- this stabilizes the projectile both during the acceleration phase and during the coasting flight through the atmosphere. There is no need for detachable sabot or other parasitic mass – the effective launch mass can be 100 %. For these reasons, the CFSM can be a breakthrough concept for both direct EM launch to orbit and EM kinetic kill weapons.

2. Development of Key Specifications

A detailed MathCad program (see attachment) has been developed to investigate the potential parameter space of the proposed launch system and to develop baseline specifications for the current project. MathCad was chosen since such programs can be (almost) read like normal documents and the performed calculations can be easily followed. All quantities in the MathCad program have physical dimensions, which allows for a simple cross check of the results. The complete program "Estimate Electromagnetic Launch Assist" is given in the Appendix. The current baseline parameter set is shown in Table 1:

The drag coefficient of a moving projectile changes with the Mach number showing a significant enhancement of drag near Mach equal to 1. A typical profile as used in the program is shown in. A more precise determination of the aerodynamic effects is given in section 4.

The electromagnetic drag depends on the details of the magnetic levitation system, which is currently not determined. We have therefore conservatively assumed that 5% of the acceleration force (without aerodynamic drag) is needed to overcome this drag. The actual value is likely to be lower.

4

Parameter	Unit	Value
Launch assist speed	m/sec	7000
Acceleration	g	5000
Deceleration	g	1000
Projectile mass	kg	5
Sled mass	kg	100
Sled drag coefficient		0.1
Sled cross section	m^2	0.5
Guideway/sled clearance	cm	2.5
Efficiency of linear motor		TBD
Track slope angle	deg	45
Electromagnetic drag	%	5
Ambient temperature	K	293
Air density	kg/m^3	1.28
Helium density	kg/m^3	0.179
Specific heat ratio - air		1.4
Specific heat ratio - helium		1.66

Table 1: Input parameters for launch assist calculations. Assumed base line parameters

The calculated performance values and requirements for the chosen input parameters of Table 1 are shown in
Table **2**.

Parameter	Unit	Value
Total mass to accelerate	kg	105
Track length for acceleration	m	499.7
Acceleration force	kN	5410
Drag force in air	kN	1570
Drag force in helium	kN	219
Total propulsion force in air	MN	6.97
Total propulsion force in helium	MN	5.63
Kinetic energy	Mjoule	2570
Drag energy in air	Gjoule	0.39
Drag energy in helium	Gjoule	0.05
Total energy in air	Gjoule	2.96
Total energy in helium	Gjoule	2.63
Peak power in air	Gwatt	48.82
Peak power in helium	Gwatt	39.38

Table 2: Calculated requirements of EMLA system for base line parameters
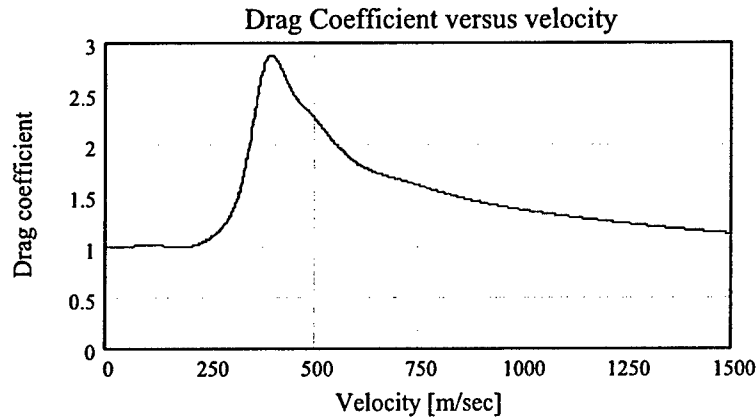
Figure 1: Drag coefficient versus velocity for a drag coefficient of 1. It is assumed for the initial estimates that the shown dependence describes the dependence of drag coefficient on velocity for our system.

2.1 Ambient Atmosphere

The MathCad program considers different gases as the ambient atmosphere, which are described by their density and their specific heat ratio γ = cp/cv. For the results shown in

Table 2 it is assumed that the ambient atmosphere consists of air or helium at normal pressure (1 atm). Different pressures can be chosen by varying the density ρ [kg/m^3] of the gas.

Equation 1

$$F_{drag} = \tfrac{1}{2} * C_{drag} * \rho * v^2 *A$$

C_{drag} : drag coefficient
ρ: density of gas
v: velocity of object (sled)
A: cross section

Since the aerodynamic drag is a significant contribution to the required acceleration force (see below) it would be of interest to reduce the pressure of the atmosphere surrounding the accelerating sled. Also this is not ruled out at the present state of the project, it could be a significant complication. The transition of the sled form a reduced pressure to the normal atmospheric pressure at the end of the track could cause a significant shock and has to be studied in more detail.

2.2 Track Length and Track Inclination

The track length required for the EMLA system depends on the launch speed and the assumed acceleration. The launch speed for the proposed system is assumed to be 7000 m/sec, which is about Mach 20 in air and Mach 7 in helium. As shown in Table 1 a track length of

6

500 m is assumed. As shown in our recent publication[1], the track has to be inclined at the track end to about 45 degrees or more for an efficient launch. This could be achieved by a straight track with constant inclination or a track that starts horizontally and bends upwards to the required angle at the end of the track. However, as shown below (Section 3), the centrifugal forces acting on a bend track would be so large that the solution would be difficult to implement and would compromise the overall system reliability. A track with constant inclination is therefore chosen for the baseline design.

A lower limit of the track length is imposed by the increased acceleration needed for shorter tracks. The sled acceleration will be supplied by a linear drive system (TBD), which becomes increasingly demanding for higher accelerations. Also the peak power requirements for the linear drive system increases with acceleration and become increasingly difficult to achieve. As a compromise between track length and acceleration we have chosen to limit the acceleration to about 5000g at the end of the track.

2.3 Deceleration Section
A deceleration section would have the advantage that a launch could be interrupted at any time, which would improve the system reliability. Such an additional track section would also (in principle) allow to decelerate the sled after the projectile has been launched and to reuse the sled for another launch. However, the deceleration section would require a significant increase in track length and cost. Also an additional linear drive system would be needed, and the track construction would significantly increase in complexity since the launch point will be at a significant height due to the track inclination.

With our present understanding of the EMLA system we think that the track solution without deceleration section is the preferred option. The cost of the track with the linear drive system is significantly lower without the deceleration, and it is not clear to which extend the sled would be reusable after a launch. The large forces and surface temperatures (see below) experienced by the sled during the acceleration could easily lead to some damage and a significant amount of inspection and repair work might be required before another launch.

2.4 Base Line Parameters and Subsystem Specifications
The subsystem specifications developed with the help of the described MathCad program are regarded as the design goals for the various subsystems of the EMLA system. The detailed analysis performed in the different project tasks might lead to modifications.

Key design requirements determined with the MathCad program are as follows:

The aerodynamic drag acting on the sled is significantly stronger for air than for helium. The dependence for air and helium at 1 atm are shown in Figure 2. The values shown in the

---

[1] **"Rocket Performance Analysis Using Electromagnetic Launch Assist"**, AIAA Aerospace Sciences Conference, Reno 2005, A. Uranga, D. Kirk and H. Guiterrez, FIT,R.B. Meinke, AML,K. Barker, Schafer Corporation

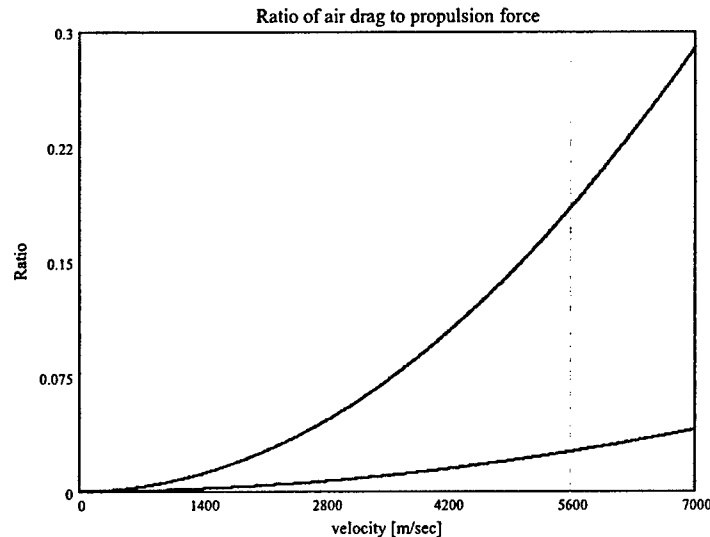figure are based on the assumed sled cross section of 0.5 m^2 and a drag coefficient of 0.1 near Mach 0.

Figure 2: **Ratio of drag to propulsion force as a function of sled velocity for air (red curve) and helium (blue) curve based on a track length of 500 m and a constant acceleration of 5000 g for a pressure of 1 atm.**

For the assumed constant acceleration of 5000 g the force necessary to overcome the aerodynamic drag is about 30% of the force needed for the acceleration alone (without aerodynamic drag) at the end of the track. The equivalent value for helium is significantly lower and amounts to less than 4%. Since the acceleration force is constant, the curves also reflect the increasing importance of the aerodynamic drag with increasing speed. A detailed analysis of the aerodynamic effects is performed in Task 3 (see below).

The importance of the aerodynamic drag on the acceleration force has been studied for various acceleration profiles. In air for constant accelerations larger than 1400 g the plotted ratio from Figure 2 is less than 1, for accelerations below 1400 g the aerodynamic drag becomes more important than the acceleration force. For helium this crossover happens for acceleration of about 200 g.

It is also of interest to point out that the peak in the drag coefficient near Mach 1, as shown in Figure 1, has very little effect on the shown drag profile. Only for launch velocities less than 500 m/sec the drag peak becomes important.

2.5 Optimization of Acceleration Profile
Due to the quadratic dependence of the aerodynamic drag on velocity (see Equation 1) the drag is largest at the end of the track. It is therefore beneficial to use an acceleration profile, which is not constant, but has the largest acceleration at the start of the track and tapers off towards the end? This would be of particular interest for air, in which the drag amounts to about 30% of the total required force at the end of the track and would even be of increased

8

importance for accelerations smaller than 5000 g. As part of the described MathCad program this optimization is performed.

For reasons of simplicity a linear acceleration profile is assumed, which starts with an initial acceleration b_{start} and falls linearly with track length during the whole cycle as shown in Equation 2.

Equation 2 $acc(s) = b_{start} + m_o * s$

> s: track length or position on the track
> m_o: slope of acceleration profile
> b_{start}:   acceleration at s = 0

For the real system the acceleration profile will most likely contain a short ramp from b = 0 to the initial value b_{start}, but this has has no significant effect on the performed optimization. Assuming the linear profile yields the following differential equation of motion:

Equation 3 $$b_{start} + m_o \cdot x = \frac{d^2}{dt^2} x(t).$$

The differential, describing the acceleration profile, can be solved analytically for velocity and position of the sled as a function of time t. The following solutions are obtained:

$$v(t) = \frac{b_{start}}{\sqrt{m_o}} \cdot \sinh\left(\sqrt{m_o} \cdot t\right)$$

Equation 4

$$x(t) = \frac{b_{start}}{m_o} \cdot \left(\cosh\left(\sqrt{m_o} \cdot t\right) - 1.\right)$$

Using Equation 4 and varying the parameters b_{start} and m_o, the acceleration profile has been optimized to make the required propulsion force independent of track position. The solution for air is shown in Figure 3 (solid red curve).

The optimized acceleration profile reduces the force required from the linear drive system, which otherwise rises towards the end of the track. Also the peak power requirements are mitigated by this approach. It might even be advantageous to choose a further reduction in the acceleration towards the end of the track, since it will be more difficult to supply the necessary acceleration force at the higher speeds.
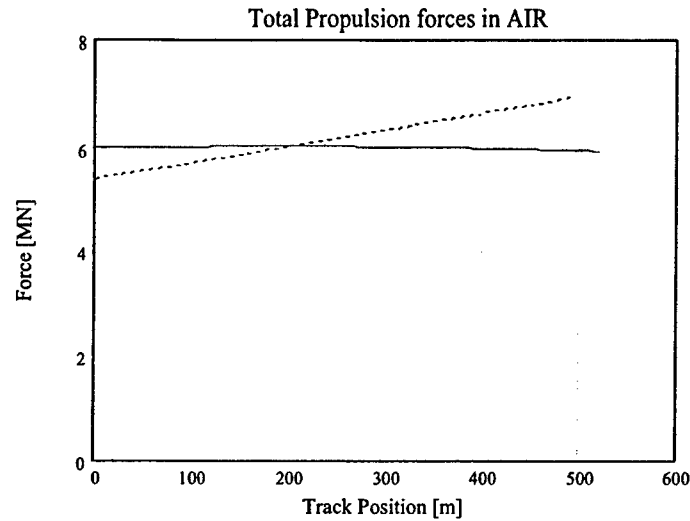
Figure 3: **Propulsion force as a function of track position in air for a constant acceleration of 5000 g (dashed curve) and a linear falling acceleration profile with b_{start} = 5550 g and an end acceleration of 4100 g.**

The corresponding propulsion force versus track position for the same acceleration profile (bstart = 5500 g and end acceleration of 4100 g) but for helium is shown in Figure 4.
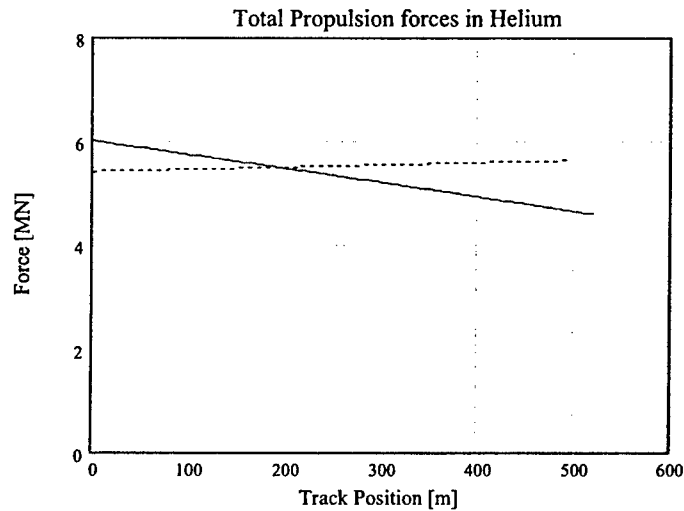

Figure 4: **Propulsion force as a function of track position in helium for a constant acceleration of 5000 g (dashed curve) and a linear falling acceleration profile with b_{start} = 5550 g and an end acceleration of 4100 g.**

The reduced force at the end of the track (shown in Figure 4) leads to a reduction in peak power and would facilitate the system design.

For Further details of the MathCad program and the performed calculations see Appendix A.

10

3. Develop Guideway Concept

As shown in the description of Table 1 a baseline value of 500 m has been chosen for the track length. To avoid a complex control mechanism in the projectile, it has to be released under a significant angle between 25 - 45 degrees or higher (the optimum launch angle is still TBD). The launch angle can be implemented by using a sloped track or having a modest bend in the track at the end or over its full length. A comparison of these two cases is shown below.

A conceptual design for a bend track is shown in Figure 5. To minimize the centrifugal forces, the track is curved over its full length and the circular arc, which starts horizontally, is truncated when it reaches 45 degrees. The arc length was chosen to be the baseline track length of 500 m. The resulting radius is 637 m. The track could be fully underground to avoid any above ground structures. The required tunnel would start at a depth of 187 m.
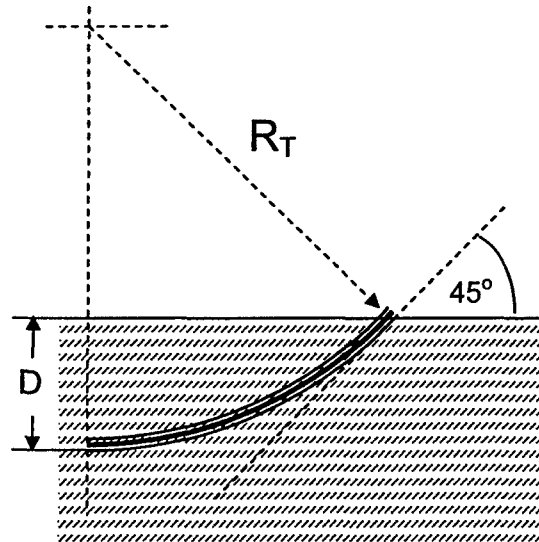

Figure 5: Conceptual implementation of a curved track

The resulting centrifugal forces acting on the track are given by Equation 5 and are shown in Figure 6:

Equation 5 $$F = m * v^2 / R_T$$

m: mass of sled with projectile
v: sled velocity
R_T: track radius

Towards the end of the track the equivalent weight acting on the track is about 800 tonnes. Although such forces could be supported, in particular in the shown concept of an underground

11

tunnel, such forces could lead to movements of the track during a launch. Under these circumstances it might be necessary to survey and realign the track after each launch. For a system requiring high reliability and responsiveness the curved solution does not seem appropriate and a straight track is preferred. A conceptual solution is shown in Figure 7.
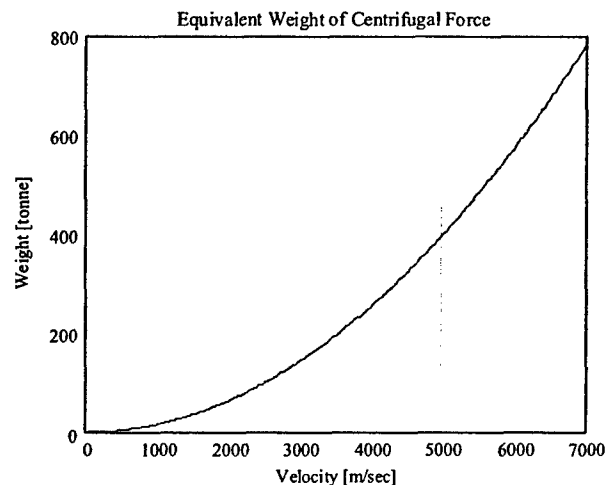

Figure 6: Centrifugal forces acting on the track as a function of sled velocity. The forces have been converted to equivalent weights (shown in tones) by dividing the force values by g = 9.8 m/sec^2.

To limit the height of the necessary support structure above ground the track is inserted over half of the length into an underground tunnel. For the baseline track length of 500 m the underground section would start 177 m below the surface.

Tunnels of the required length with the necessary underground facility do not constitute a major technical challenge. Existing tunnels for high energy physics accelerators (e.g. the Large Hadron Collider (LHC) tunnel at the European Center for Nuclear Research, Geneva, Switzerland is more than 30 km in length with much larger underground facilities).

A conceptual layout of the required launch facility is shown in Figure 8.

It is of interest to point out that the proposed launch concept would also be applicable to a canon-like launch system in which the launch speed is reduced to about Mach 2. Such a launch velocity should be sufficient for shooting the sled with payload for a few hundred miles (TBD). The centrifugal forces for such a system would be rather modest (equivalent weight of about 15 tonnes for same track length and radius), and the bend track emerging from an underground facility or a even a ship might be an attractive solution.
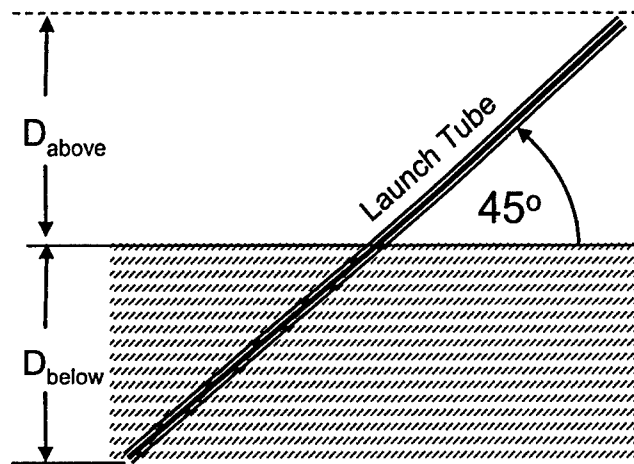
12

Figure 7: Conceptual implementation of straight track partially built into underground facility.
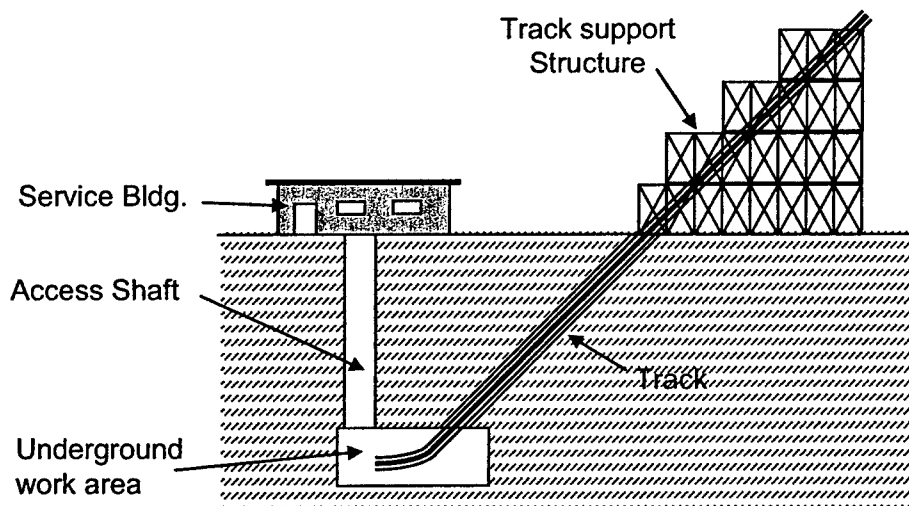

Figure 8: Conceptual layout of launch facility.

As worked out in detail in Section 6, the track has to operate under a helium atmosphere of reduced pressure. This requires a tube, which is sufficiently leak tight and can sustain the outside pressure. Although the details are beyond the scope of this project, we don't regard this requirement as a major technical challenge.

4. Description of the CFSM Launch Tube Concept

The rail gun is the EM launch technology that has received the most attention in recent years. Rail guns have several attractive characteristics but also some unresolved challenges, mostly given by the complex contact phenomena between rails and armature at very high speeds, as well as the significant heat dissipation associated to each launch, which results in damage to the gun's insulation that substantially limits the rate of fire and the overall survivability of the gun. Coaxial induction launchers have some desirable advantages over other EM launch methods in that no direct electrical contact is required, but pulsed induction motors or coil guns that can provide the required thrust force for hypervelocity applications would need to induce very large currents in the projectile - the resulting ohmic losses would lead to unmanageable heat loads and thermal destruction of the projectile.

In order to overcome the outlined difficulties with existing propulsion systems a novel concept called "Constant Flux Synchronous Motor" (CFSM) has been developed under this grant. This motor concept delivers the required propulsion forces without inducing any significant eddy currents in neither projectile nor launch vehicle. To avoid inducing significant eddy currents, the projectile coils have to see an almost constant magnetic flux during launch, a requirement that has never been met in any existing system. The CSFM launch system consists of the following components:

a) Normal conducting coils on the stationary track, pulsed with 30 to 100 kA during launch depending on the number of turns in the windings. The pulses are synchronized with the moving projectile by an appropriate hardware trigger. Near-constant flux seen by the projectile is essential to the CFSM concept. A change in flux in the projectile's coils would induce a voltage that would create eddy currents in the coil's substrate. The resulting ohmic heating could quench or even destroy the projectile's coils.

b) Superconducting coils on the projectile, operated in persistent mode (30 to 50 kA, depending on the number of turns). The coils are inductively charged prior to launch - no additional power is needed to maintain the DC currents in the projectile coils.

c) Independent pulsed power supplies connected to the launch track coils. Current in the launcher coils follow programmed pulse shapes (rise time, fall time and pulse duration) triggered by the position of the projectile along the track. The shape of the current pulses is calculated off-line - they depend on the instantaneous geometric relationship between track and projectile coils. The pulsed power supplies can be implemented as 2 or 3 combined Marx generators charged with individually controlled voltages and discharged with individually controlled delays for each track coil, in a way that pulse shapes can be adjusted to the required waveforms.

d) An energy storage system with sufficient storage capacity and power rating. There are several qualified technologies that could be used (e.g., batteries, capacitors or superconducting magnetic energy storage devices). Since the heat dissipation is substantially smaller than in other EM technologies, and the effective mass fraction can be 100%, the energy and power requirements are advantageous compared to other EM launch technologies.

14

Figure 9:
A longitudinal section of the CFSM launcher. PB: Basic cell length of CFSM system = 2 M×PT ,
for some integer M. The distance between the rear coil TR1 and the corresponding front coil TF1
is M×PT. PP: distance between coils in the projectile, PT: distance between coils in the track.
Super-indexes (p) and (n) denote coils of the previous and next track sections to be fired.

Conventional coaxial launchers rely on either external power supplies that feed the projectile through brushes, or induced eddy currents. These technologies have inherent limitations in the maximum speeds they can provide. In a DC coaxial launcher this is given by the wear and contact phenomena in the projectile's brushes, as well as ohmic heating of the projectile. In an induction launcher, inductive heating of the projectile is a limiting factor.

In a conventional pulsed coil gun, the change in speed of the projectile during launch is accommodated by increasing either pole pitch or input frequency or both along the track. In the CFSM, the sequence of pulses supplied to the track coils forms a traveling wave that determines the speed of the projectile. Since there are no iron cores in the system, the pulse shapes required to produce constant flux as seen by the projectile coils depend solely on the geometric relationships of track and projectile and can be analytically calculated off-line.

4.1 CFSM Launch Track Layout

The interaction between the track and projectile coils provide the required propulsion forces as well as self-centering suspension forces. Projectile stabilization during launch is achieved both by the self-centering action of the electromagnetic forces and by spinning the projectile prior to launch. The use of a low pressure environment in the track will minimize drag and heat transfer during launch. The schematic layout of the CFSM launcher is shown in Figure 9. The basic cell of the launch tube consists of M "rear" coils (T_{R1}, T_{R2}, ... T_{RM}) and M "front" coils (T_{F1}, T_{F2}, ... T_{FM}). The "rear" coils of such a section are pulsed with opposite current direction than the "front" coils. The distance between track coils P_T is the distance where $\dfrac{\partial M}{\partial x}$ (the gradient of M with respect to x) is maximum. This is calculated off-line and depends only on the launcher geometry.

15

The force between the projectile coil P and the track coil T is given by: $F = i_P i_T \dfrac{\partial M}{\partial x}$. The force is attractive when both currents are in the same direction and repelling when the currents have opposite directions. While the projectile coils are repelled from the nearest (active) track coil, the current pulse in the track coil increases in such a way that it keeps the magnetic flux seen by the projectile approximately constant until the projectile reaches the next track coil. At this moment in time the current pulse in the active track coil rapidly goes to zero and the next track coil is pulsed in such a way that the flux through the projectile stays (approximately) constant. Synchronization is achieved by hard-wiring the firing circuits of individual energy storage elements to sensors that detect the position of the projectile along the launch tube.

In Figure 9:

• The projectile coil currents i_{PR} and i_{PF} are constant (persistent mode superconducting currents) and both have the same current direction.

• Each track coil is connected to an independent pulse power supply which is able to supply a pre-determine pulse shape. Only two track coils are ON at any given time. In the picture, T_{R1} and T_{F1} (in red) are currently being pulsed. Triggering the track coils is hardware-controlled by proximity switches that detect the presence of the projectile.

• The "rear" pulse $i_{R1}(t)$ starts when the projectile coil P_R reaches $x = -P_T$ and ends when P_R reaches $x = 0$. The coordinate x is relative to the coordinate system that moves with the projectile. Similarly, the "front" pulse $i_{F1}(t)$ is only ON while the front projectile coil P_F is traveling through the front shaded area. The current pulses $i_{R1}(t)$ and $i_{F1}(t)$ are calculated off-line as described in the next Section. The rear coil pulls the projectile to the right (currents in the same direction) while the front coil pushes it to the right (currents have opposite directions).

• After a section is fired, the next section starts $(T_{R1}^{(n)}, T_{R2}^{(n)}, ...)$. Notice that the "front" coils of the previous section fired are placed in close proximity to the "rear" coils of the current section $(T_{R1}$ with $T_{F1}^{(p)}$, T_{R2} with $T_{F2}^{(p)}$, ..., and also $T_{R1}^{(n)}$, with T_{F1}, $T_{R2}^{(n)}$ with T_{F2}, etc.).

• For a slender projectile (i.e. length >> diameter), it is assumed that the effect of a "front" track pulse on the rear shaded section is negligible. Similarly, the effect of the "rear" track pulse on the front shaded section is negligible too.

• The mutual inductance $M(x)$ between the projectile coil and the track coil that are interacting at any given moment (in the picture, PR with T_{R1}, and PF with T_{F1}) is a function of the instantaneous axial position "x" and the basic launcher geometry (launcher diameter, projectile diameter, and air gap). Since there are no iron cores, $M(x)$ is easily and accurately calculated off-line.

Coils T_{R1} and T_{F1} are fired at the same time, when $x = -P_T$. When $x = 0$, T_{R1} and T_{F1} are turned OFF. The origin of the coordinate system "X" moves to T_{R2}. At the same time, the pulses in T_{R2} and T_{F2} start. Again, the "rear" currents are fired in the same direction as the projectile current, whereas the "front" coils are fired in opposite direction. This way, the rear coil is always pulling the projectile forward while the front coil is pushing. T_{R2} and T_{F2} are turned OFF when the local coordinate x reaches zero. The sequence is repeated until the last coils of the section T_{RM} and T_{FM} are fired. The next section $(T_{R1}^{(n)}$ and $T_{F1}^{(n)}$, $T_{R2}^{(n)}$ and $T_{F2}^{(n)}$,

16

...) fires in similar manner. Notice that the coils in the "front" section always fire in direction opposite to the projectile coil currents, and so on. If a given pulse shape is difficult to achieve with a single pulse source or Marx generator, two or three can be operated in parallel to obtain the required pulse shape by superposition. Some pulse characteristics (i.e. rise time) are given by track parameters such as number of turns (i.e., inductance) of a given coil.

4.2 Analytical Overview of the CFSM Concept

As described in the previous section, the only track coils active at any given time are the two located immediately ahead (T_{RI}) and immediately behind (T_{FI}) of the projectile rear and front coils, respectively. The corresponding current pulses last only while coils P_R and P_F are moving within their corresponding shaded areas. The time taken to travel the shaded subsection P_T is t_{PT}.

The magnetic field and flux acting on the projectile coils P_R and P_F while traveling within the shaded areas (see Figure 9) will be considered. A simpler case will be analyzed first: pitch and yaw angles are assumed to be small, and the centers of coils P_R and P_F are considered near the axis of symmetry of the launch tube. In this case, the magnetic field B produced by the track coils T_{RI} and T_{FI} on any circular concentric path within the surfaces enclosed by P_R and P_F has cylindrical symmetry (i.e., B is the same for all points along any concentric circular path within the surfaces enclosed by P_R and P_F). The flux ϕ caused by the track coil T_{RI} on the surface enclosed by P_R can therefore be calculated using circular differential elements as shown in Figure 10.
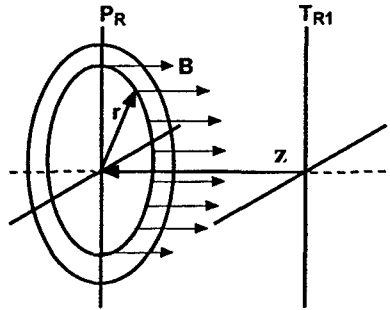
Figure 10: Magnetic Flux through a Projectile Coil section.

The flux ϕ caused by the track coil T_{RI} on the surface enclosed by P_R is:

$$\phi = \int_A BdA \cong \sum_{k=0}^{N} B(2\pi k\Delta r)\Delta r,$$ where B is some nonlinear function of the geometry and the

current i_{RI}, $B = i_{RI}g(r,x)$, and $r = k\Delta r$ is the discretized version of the continuous variable r. The index k numbers the concentric rings used in this numerical approximation. The field of the projectile coil P_R is not included on the flux calculation since it's a stationary constant field that travels with the projectile and therefore causes no induction $\varepsilon = -\dfrac{d\phi}{dt}$ on the projectile's coil. The condition for near-constant flux on the projectile coil P_R traveling in the rear shaded area of Figure 1 can now be written as:

17

$$2\pi \sum_{k=0}^{N} i_{R1}(t) g(k\Delta r, x)(k\Delta r)\Delta r + 2\pi \sum_{k=0}^{N} i_{F1}(t) g(k\Delta r, x + MP_T)(k\Delta r)\Delta r = \Phi_0 \tag{1}$$

which includes the effect of the two track coils being pulsed (T_{R1} and T_{F1}, with currents $i_{R1}(t)$ and $i_{F1}(t)$) on the rear projectile coil P_R. $M \times P_T$ is the distance between coils T_{R1} and T_{F1} (the length of a basic track section is $2M \times P_T$) and Φ_0 is some characteristic flux to be kept near constant. For a slender projectile (i.e., the projectile radius R_P is much smaller than the length of the half-section $M \times P_T$), this can be simplified by neglecting the effect of the front track coil T_{F1} (which is rather far away) on the rear projectile coil P_R:

$$2\pi \sum_{k=0}^{N} i_{R1}(t) g(k\Delta r, x)(k\Delta r)\Delta r \cong \Phi_0, \quad -P_T < x < 0 \tag{2}$$

and $\Delta r = \dfrac{R_P}{N}$, where N is an arbitrarily large integer. This can be regrouped as:

$$\sum_{k=0}^{N} i_{R1}(t) g(k\frac{R_P}{N}, x)k \cong \frac{\Phi_0}{2\pi \left(\dfrac{R_P}{N}\right)^2}, \quad -P_T < x < 0 \tag{3}$$

The time taken to travel the shaded subsection (t_{PT}) is discretized as $t = j\Delta t$, where $\Delta t = \dfrac{t_{PT}}{M_t}$ and M_t is some (large) integer, $j=0 \dots M_t$. The required current pulse $i_{R1}(t)$ at time $t = j\Delta t$, must meet the near-constant flux condition (3):

$$\sum_{k=0}^{N} i_{R1}(j\Delta t) g\left(k\frac{R_P}{N}, x(j\Delta t)\right)k \cong \frac{\Phi_0}{2\pi \left(\dfrac{R_P}{N}\right)^2}, \quad -P_T < x < 0 \tag{4}$$

where $x = x(j\Delta t)$ is the position of the projectile coil P_R relative to the coordinate system T_R at the present moment. In this expression, the required current pulse $i_{R1}(t)$ does not depend on the integration variable k, and can therefore be factored out of the summation above. This yields:

$$i_{R1}(j\Delta t) \cong \frac{\Phi_0}{2\pi \left(\dfrac{R_P}{N}\right)^2 \sum_{k=0}^{N} g\left(k\frac{R_P}{N}, x(j\Delta t)\right)k} \tag{5}$$

for $-P_T < x < 0$, which illustrates how the desired current pulse $i_{R1}(t)$ is a function of the instantaneous position $x = x(j\Delta t)$, and $g(r, x)$, that depends on the geometric relationship of track and coil. The current $i_{R1}(t)$ and the position $x = x(j\Delta t)$ are related in this model through Newton's second law and the electromagnetic thrust forces:

$$F_x = m\ddot{x} \approx i_{R1}(t) i_{PR} \frac{\partial M}{\partial x}\bigg|_x + i_{F1}(t) i_{PR} \frac{\partial M}{\partial x}\bigg|_{2P_T + x} \tag{6}$$

18

for $-P_T < x < 0$, where m is the projectile's mass, i_{PR} is the projectile coils current (a constant) and the gradient $\dfrac{\partial M}{\partial x} = f(x)$ can be calculated off-line and interpolated as a function of the projectile's position x. In the launch tube's low-pressure atmosphere the aerodynamic drag can be neglected and therefore the total force in the x direction is determined by the electromagnetic thrust forces. The dynamic dependence of current, force and position can be described by converting the algebraic condition (5) into a differential condition in time. Taking the derivative of Equation (3) with respect to time, yields, for $-P_T < x < 0$:

$$\sum_{k=0}^{N} \frac{di_{R1}(t)}{dt} g(r,x)k + \sum_{k=0}^{N} i_{R1}(t)\left(\frac{\partial g}{\partial r}\dot{r} + \frac{\partial g}{\partial x}\dot{x}\right)k = 0 \tag{7}$$

where $r = k\dfrac{R_P}{N}$. A similar equation can be written for the front coil current $i_{F1}(t)$. Since both $i_{R1}(t)$ and its time derivative are independent of the summation variable k, this equation can be rearranged as follows:

$$\frac{di_{R1}(t)}{dt} = -i_{R1}(t)\frac{\sum\limits_{k=0}^{N}\left(\dfrac{\partial g(k\frac{R_P}{N},x)}{\partial x}\dot{x}\right)k}{\sum\limits_{k=0}^{N} g(k\frac{R_P}{N},x)k} \tag{8}$$

where the projectile speed is large ($\dot{x} \gg \dot{r}$) and therefore the term $\dfrac{\partial g}{\partial r}\dot{r}$ in (7) can be neglected. The corresponding expression for the front coil is:

$$\frac{di_{F1}(t)}{dt} = -i_{F1}(t)\frac{\sum\limits_{k=0}^{N}\left(\dfrac{\partial g(k\frac{R_P}{N},2P_T+x)}{\partial x}\dot{x}\right)k}{\sum\limits_{k=0}^{N} g(k\frac{R_P}{N},2P_T+x)k} \tag{9}$$

Equations (6), (8) and (9) define the dynamic relationship between the track pulses $i_{R1}(t)$, $i_{F1}(t)$ and the projectile's motion. The coupled equations can now be described as a system of four nonlinear ordinary differential equations of the four state variables:

$$z_1(t) = i_{R1}(t), \quad z_2(t) = i_{F1}(t), \quad z_3(t) = x, \quad z_4(t) = \dot{x}$$

$$\frac{d\vec{z}}{dt} = \vec{F}(\vec{z},t) \tag{10}$$

19

$$
\begin{bmatrix} dz_1/dt \\ dz_2/dt \\ dz_3/dt \\ dz_4/dt \end{bmatrix} = \begin{bmatrix} -z_1 z_4 \dfrac{\displaystyle\sum_{k=0}^{N} \left(\dfrac{\partial g(k\frac{R_P}{N}, z_3)}{\partial z_3} \right) k}{\displaystyle\sum_{k=0}^{N} g(k\frac{R_P}{N}, z_3)k} \\ -z_2 z_4 \dfrac{\displaystyle\sum_{k=0}^{N} \left(\dfrac{\partial g(k\frac{R_P}{N}, 2P_T + z_3)}{\partial z_3} \right) k}{\displaystyle\sum_{k=0}^{N} g(k\frac{R_P}{N}, 2P_T + z_3)k} \\ z_4 \\ z_1 \dfrac{i_{PR}}{m}\dfrac{\partial M}{\partial z_3}\bigg|_{z_3} + z_2 \dfrac{i_{PR}}{m}\dfrac{\partial M}{\partial z_3}\bigg|_{2P_T+z_3} \end{bmatrix}
\qquad (11)
$$

The coupled system of ordinary differential equations (11) can be readily solved using standard numerical techniques such as the Runge-Kutta-Fahlberg or Adams-Moulton algorithms, starting at the initial conditions:

$$
z_1(\varepsilon) = i_{max}, \quad z_2(\varepsilon) = Gi_{max}, \quad z_3(\varepsilon) \approx -P_T, \quad z_4(\varepsilon) \approx \dot{x}_0 \qquad (12)
$$

where ε is the (hardware given) shortest time in which the energy storage devices can discharge the maximum current peak i_{max}, and $\dot{x}_0$ is the projectile velocity at the end of the previous track segment (ε is typically very small compared to the total duration of the pulse t_{PT}). The numerical solution of (11) subject to (12) ends when $z_3 = 0$, yielding the current waveforms $i_{R1}(t)$, $i_{F1}(t)$ that generate maximum thrust in the launch vehicle while keeping a near-constant flux region that travels synchronously with it. Notice that for the rear coil solution, the initial condition is $i_{R1}(\varepsilon) = i_{max}$, whereas for the front coil $i_{F1}(\varepsilon) = G\ i_{max}$ where $0 < G < 1$ is a constant to be optimized by successive solutions of (11) subject to (12).

3.2.1 Computation of Mutual Inductance

To estimate the electromagnetic forces (thrust, drag and guidance) acting on the projectile during launch, the conductors in the track and projectile coils are first approximated by infinitely thin, circular filaments. This approximation is sufficient at the conceptual design stage and will be improved during Phase 2 to include the effect of conductor thickness. The magnetic field generated by a circular filament conductor is given by:

20

$$B_r(r,z,a) = \frac{I\mu_0}{2\pi} \cdot \frac{z}{r\sqrt{(r+a)^2 + z^2}} \cdot \left[K(r,z,a) - \frac{(r^2 + a^2 + z^2)}{(r-a)^2 + z^2} \cdot E(r,z,a) \right]$$

$$\text{(13)}$$

$$B_z(r,z,a) = \frac{I\mu_0}{2\pi} \cdot \frac{1}{\sqrt{(r+a)^2 + z^2}} \cdot \left[K(r,z,a) - \frac{(r^2 - a^2 + z^2)}{(r-a)^2 + z^2} \cdot E(r,z,a) \right]$$

where B_r and B_z are the radial and axial component of the magnetic field, a is the radius of the wire loop, I is the current in the loop and μ_0 is the permeability of free space ($4\pi \times 10^{-7}$ volt sec/A.m). K and E are the first and second kind of elliptical integrals:

$$K(r,z,a) = \int_0^{\pi/2} \left[1 - \frac{4ar}{(r+a)^2 + z^2} \cdot \sin\theta \right]^{-\frac{1}{2}} d\theta$$

$$\text{(14)}$$

$$E(r,z,a) = \int_0^{\pi/2} \left[1 - \frac{4ar}{(r+a)^2 + z^2} \cdot \sin\theta \right]^{\frac{1}{2}} d\theta$$

where r and z are the polar coordinates of any point in space where the magnetic field is calculated. Computation of the electromagnetic forces requires an estimate of the mutual inductance between the coils in the track and the corresponding coils in the projectile, as shown in Eq. (6). The basic computation of mutual inductance is for two filament loops in space, i.e., it is assumed that the depth of penetration of the magnetic field in the filament is equal or greater than the diameter of the filament, or, in other words, that the current density in the filament is constant.
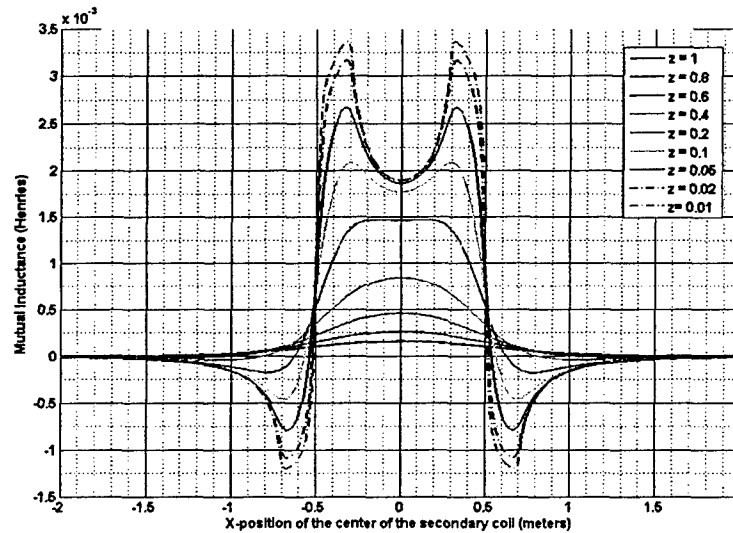
Figure 11: Mutual inductance versus radial displacement for various axial positions (Z)

21
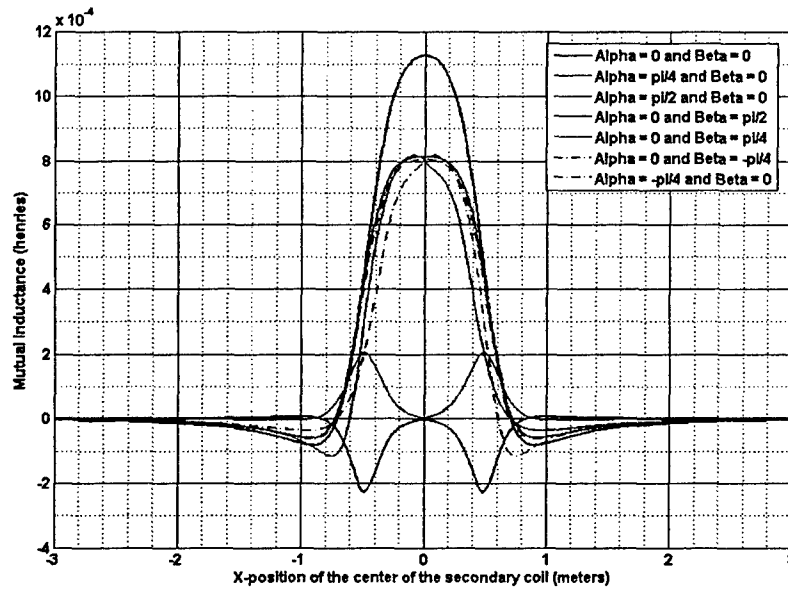
Figure 12: Mutual inductance (M) versus radial displacement for various angles of rotation of the secondary

Two angles (Alpha and Beta) define the tilt of the moving coil relative to the fixed coil. The coil's mesh can now be expressed relative to the fixed coil for any rotation of the secondary. Rotation around the Z-axis is not considered due to axial symmetry.

The magnetic field is calculated on every point on the secondary's mesh: both radial (B_r) and axial (B_z) components are found in the fixed coordinate system attached to the primary. To calculate the flux, the component of the field perpendicular to secondary surface is calculated, using the inverse of the rotational matrices M_{01} and M_{12}. The flux through the projectile coil is defined as the sum of all normal components of the magnetic field expressed in the coordinate system 2. The flux, divided by the current in the primary coil, gives the mutual inductance. Several geometric configurations were simulated, using R_p(primary) = 0.5 m, R_s (secondary) = 0.2 m. and theta varies from 0 to 2π with a step of 0.1 rad. The radial coordinate r varies from 0.01 to R_s with a step of 0.01 m. Figure 11 shows the mutual inductance as a function of the transverse motion (secondary and primary move in parallel planes for different axial positions). Alpha, Beta and the y were set to 0. As the axial distance increases, the mutual inductance decreases as expected. For small axial distance between primary and secondary, the mutual inductance has two peaks and a local minimum. This behavior is related to the local curvature of the magnetic field, which is more important at smaller axial distances. Figure 12 shows the effect of the rotation angles. The axial position is set to 0.3 m with respect to the center of the primary coil, and a transverse motion in the radial direction is simulated. The resulting mutual inductance is plotted for various rotation angles.

As expected, the mutual inductance is higher when Alpha and Beta are equal to 0 (the flux linkage is maximal). For Alpha = 0 and Beta = 0, M is near zero, except when the secondary is near the edges of the primary, in which case the magnetic field has a strong local curvature around the edges, i.e., a substantial component that generates flux. Similarly, when Alpha = 0

22

and Beta= $\pi/2$. Depending on the axial position, the mutual inductance might be negative, since the flux depends on the local curvature of the magnetic field.

Figure 13 shows the evolution of the mutual inductance as a function of axial displacement between the two coils for various radial displacements. For the case shown, Alpha and Beta are zero. As expected, the mutual inductance is symmetrical with respect to Z=0 and maximal when the two coils are in the same plane. The mutual inductance increases with radial off-set. No sign change of the mutual inductance is expected as function of axial position.
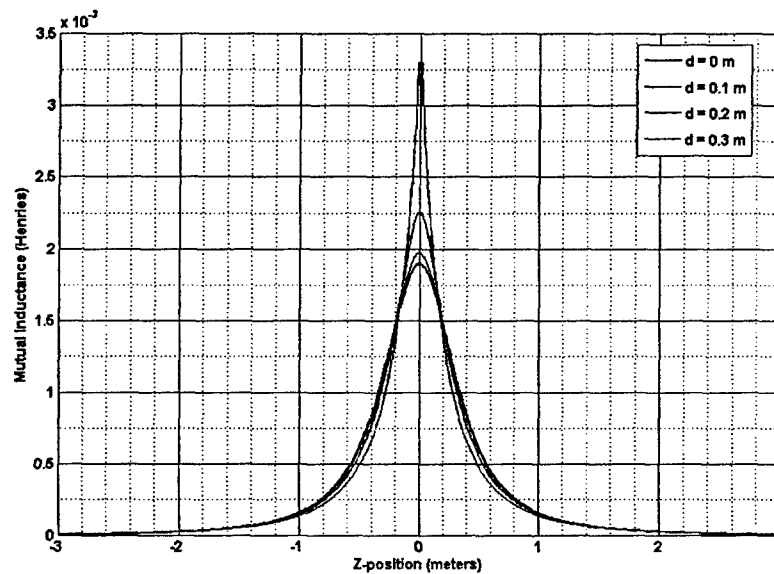
Figure 13: Mutual inductance (M) versus axial displacement (Z), for various center offsets d between the two loops.

5. Persistent Current Superconducting Coils

As described in Section 4, the propulsion system requires secondary coils on the projectile that interact with the pulsed coils on the launch tube track. The operational current of the projectile coils is estimated to be 30 to 50 kA. The mutual inductance between the track and projectile coils has to be as large as possible to achieve the necessary propulsion forces of about 5 MN (Table 1). The required currents of the projectile coils are sustained by superconducting ring coils mounted coaxially on the projectile as shown in Figure 14.

Superconductivity is the breakthrough technology that allows large current in the projectile without brushes, external connections or the heat load typically associated to large currents. Superconducting coils have practically zero resistance ($\sim 10^{-9}$ ohm), which is essential to avoid excessive heat loads at the required operational currents (up to 50 kA). These superconducting coils are operated in a persistent mode and no power supply is required during launch. With an estimated resistance of per coil of 10^{-9} ohm, the heat load at 50 kA is only 2.5 W.

The projectile could be launched as a single object (no separation required after launch) or could detach after launch, if used to deliver a payload such as a laser propulsion engine (see Figure 14, left). This flexibility permits to reach 100% effective payload mass as desired in kinetic kill applications.

The superconducting rings are charged inductively to the required operational current prior to launch. The individual superconducting wires or tapes are inserted in a sturdy metallic conduit filled with cryogen (most likely helium or hydrogen) to cool the superconductor to its required operational temperature. Prior to a launch, the coil conduits would be connected via umbilical cords (small cryogenic transfer lines) to a refrigerator, cooled to the operational temperature and filled with a certain amount of cryogen. The umbilical cords are disconnected shortly before the launch, and the superconductor is kept at the operational temperature by the amount of cryogen inside of the conductor conduit. Since the launch duration is only about 0.5 seconds (see Table 1), aerothermal heating is estimated to be about 50 K in the surface of the projectile (see section 6) for a Mach 20 launch speed, with insignificant induction heating during launch (see Section 4). Therefore, a small amount of cryogen is sufficient to keep the conductor in the superconducting state.

Under these operational conditions, the cryostat surrounding these coils can be simple and inexpensive. While cryostats for most applications require a careful reduction of external heat loads, the cooling requirements for this application are rather modest. The launch tube low-pressure atmosphere will function as an insulation vacuum, and very little convective heating from the surroundings is expected.

Placing LTS superconductors in metallic conduits is well established technology, widely used in pulsed fusion magnets. The direct contact between the superconductor and the cryogen in this cable-in-conduit (CICC) technology, enables that energy dissipated from pulsed magnetic fields or conductor motion is absorbed by the cryogen. A typical superconductor with a current carrying capacity of about 50 kA is shown in Figure 15.
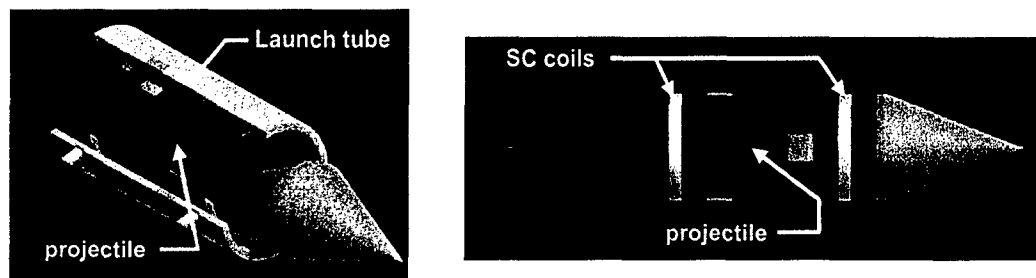
Figure 14: left) Layout of projectile inside a section of the launch tube, when used as first stage to launch a laser propulsion engine. right) Projectile with superconducting rings
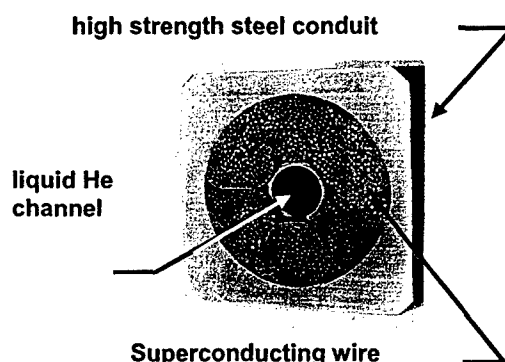

Figure 15: Cable-in conduit used on the ITER CS Model Coil. The conduit dimensions are ~ 50 × 50 mm. This CICC conductor operated successfully at 46 kA and 13 Tesla, at a magnetic field pulse rate of 2 Tesla/sec.

While the specific heat of almost all materials is extremely low at temperatures of about 4.5 K ($\leq$ 1 Joule / (kg K)), the specific heat of helium peaks at this temperature and reaches values of more than 8000 Joule / (kg K). Due to its large specific heat at these temperatures, helium can absorb significantly larger amounts of heat without significant temperature rise.

The specific heat of low temperature superconductors at typical operational temperatures of 4.5 K is also very low - these metallic alloys cannot absorb significant amounts of heat without heating up above their critical temperature and becoming normal conducting. On the other hand, BSCCO, YBCO and MgB_2 high temperature superconductors (HTS) are already available in wire and tape form. If operated at temperatures below 20 K, these conductors can carry large currents at rather high magnetic fields. BSCCO-2212, and MgB_2 operated at 4.5 K, have a much higher critical field than any low temperature superconductor (LTS). While not absolutely necessary for the proposed launcher application, HTS conductors would offer a much higher energy margin and therefore quench safety than LTS conductors. The amount of heat that can be accommodated in HTS conductors can exceed those of LTS by a factor of several thousand. This is due to the much higher enthalpy of materials at higher temperature and the much larger gap between operational temperature and critical temperature. HTS superconductors, operating at 20 to 30 K, therefore offer a much higher safety margin between

25

nominal operation and quench compared to LTS superconductors operating at liquid helium temperatures (typically 4.5 K).

On the other hand, the critical currents of HTS superconductors (YBCO and BSCCO) can be pressure sensitive and their operation under large stress levels has not been well established. Specific tests will be required to qualify these conductors for the launcher application. Appropriate tests will be proposed for a second Phase of this project.

6.   Aerodynamic and Aerothermal Effects

During the Phase I effort, significant progress has been made on understanding and modeling the aerodynamics and heat transfer of the sled/projectile system while contained within a launch tube. The calculations have been performed using both closed-form analytical solutions as well as using numerical calculations.

Employing an evacuated launch tube (~ 1/100th of an atmosphere) the aerodynamic forces, i.e. lift, drag and moments, are within manageable levels, which can easily be compensated for by the electromagnetic forces. For example, the lift and drag are on the order of 1-15 kN and the moments at maximum misalignment of the projectile allowed by the launch tube are around 20 kN m. A parametric study has been performed over a range of Mach numbers and projectile orientations. Since the geometry of the sled/projectile has changed to a conical/cylindrical shape during the course of this investigation, a new analytical and computational study was completed for this shape, and the resultant lift, drag and moments being of the same order of magnitude as the flat plate approximation or less due to a three-dimensional relieving effect associated with the conical shape. A table of drag and lift coefficients is presented later in this section.

Although aerodynamic forces and moments are easily overcome by magnetic forces within the launch tube at relatively modest vacuum levels, it has been found that 1/100th of an atmosphere vacuum is essential to alleviate heat transfer concerns within the launch tube. Using stainless steel as the sled material, a series of simulations were conducted to ensure that the material would not approach melting temperatures. The cases were performed by evaluating the heat flux along the surface of the projectile during a 0.5-second simulated acceleration from zero to 7 km/s. Even using worst case, constant heat flux it was found that the surface temperature of the stainless steel body only increases by about 50 K, if the pressure within the launch tube is kept to 1/100th of an atmosphere. To summarize, the preliminary studies have indicated that the level of vacuum required is governed by heat transfer considerations rather than the need to minimize aerodynamics disturbance forces within the launch tube. Heat transfer within the launch tube was also investigated using computational methods which are coupled to the flow solution.

In order to understand the aerodynamics of a projectile traveling at supersonic and hypersonic speeds in the channel of an electromagnetic launcher, numerical simulations were performed using the Computational Fluid Dynamics (CFD) commercial state-of-the-art code FLUENT version 6.2. In this section, the main results of two-dimensional simulations are presented and analyzed.

6.1 Analysis of a Simpler Case: Diamond-Shaped Projectile in a Large Channel

The purpose of this section is to provide a qualitative understanding of the key phenomena involved in supersonic flows, namely shocks and expansion fans. Consider a projectile with a diamond shape, ~0.63 m long and 0.04 m thick, its length and thickness being the same as the baseline sled. The walls of the channel are placed sufficiently far from the projectile so that the reflected shocks and expansion waves do not touch the projectile. The projectile is traveling at Mach 2 in air at 1 atm (101325 Pa) and 300 K, and the fluid is assumed inviscid for this preliminary case. The grid for the simulation is obtained through adaptive refinement and can be seen in Figure 16.

The velocity, pressure, density, and temperature fields around the projectile are shown in Figure 17. An oblique shock appears at the leading edge of the projectile across which velocity decreases while pressure, density, and temperature increase; a shock represents a discontinuity in the flow properties. From the upper and lower corners of the shape, an expansion fan emanates to turn the flow. The flow properties change continuously across the fan: velocity increases while pressure, density, and temperature decrease. The drag force on the projectile is the result of the difference in pressure between the front half and back half of the shape. Because of the expansion wave, the pressure in the front will be higher than the pressure in the back, and hence a net aerodynamic force acts backwards.

Finally, as can be seen in Figure 17, both shocks and expansion waves are reflected by the channel walls. The main effect of the interaction between the expansion fan and the shocks is the bending of the shock away from the fan. As will be emphasized in the following sections, even though the bending angle is relatively small, this interaction can have important consequences on the overall aerodynamic force on the projectile by changing the location where the reflected shock will encounter the projectile again.
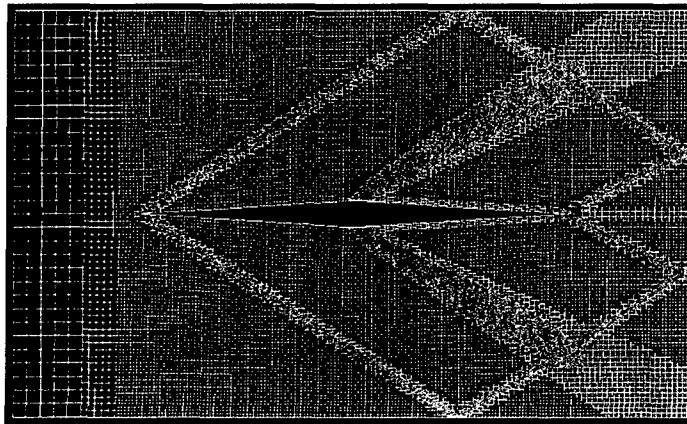
Figure 16: Grid used for the diamond-shaped projectile in inviscid flow

(a) Velocity

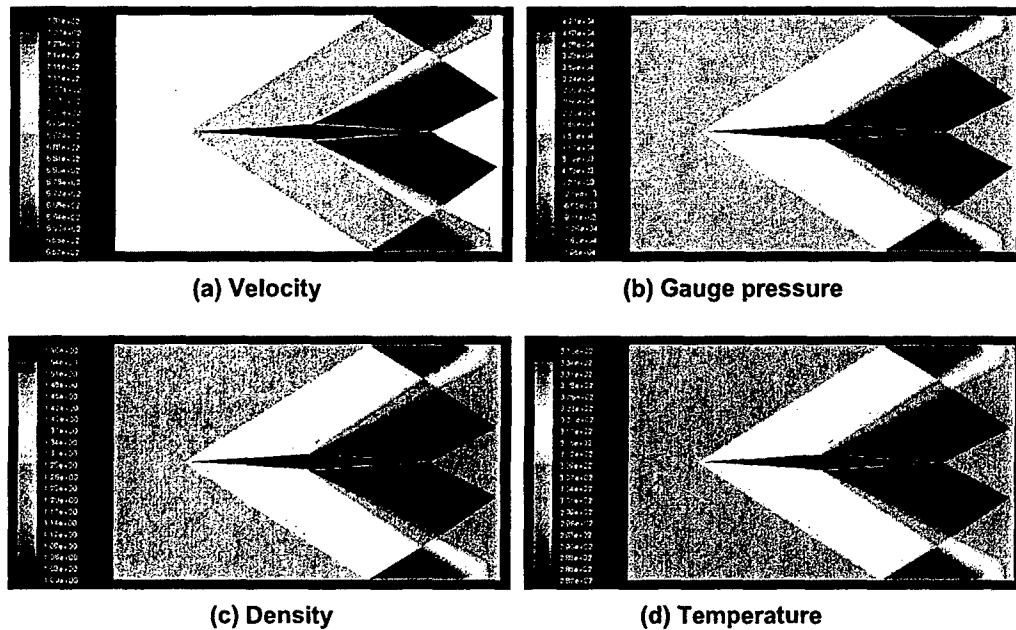(b) Gauge pressure

(c) Density

(d) Temperature

Figure 17: Velocity (a), pressure (b), density (c), and temperature (d) fields for the inviscid flow around a diamond-shaped projectile traveling in air at Mach 2.

6.2 Projectile Traveling in a Narrow Channel

The viscous supersonic/hypersonic flow through a very narrow gap between two walls is extremely difficult to simulate mainly because
- the flow is highly energetic and highly compressible;
- each time a shock reflects off a wall it interacts with the boundary layer, resulting in a very complex physical phenomena;
- the turbulence models that need to be used to simulate turbulent flows are accurate near wall because they rely on "classical" boundary layer theory, but they are often inadequate for use in shock-boundary layer interactions.

Because of these issues, the numerical simulation has problems capturing the physics of the flow and is hence very unstable (i.e. it tends to diverge). In the design baseline the gap between the sled and the track is 1cm, the sled being 4 cm high. The supersonic/hypersonic flow in this tiny channel was not possible to simulate accurately. Therefore, for the computational fluid dynamics study, the gap was increased to 8cm, which corresponds to a launcher channel of 10cm radius. The fluid is taken to be helium and assumed to behave like an ideal gas.

The purpose of this analysis is to aid in the development of a simplified semi-empirical model that will describe the main features of the flow and predict the aerodynamic drag, lift, and moment on the projectile at any instant during its flight inside the launcher. The starting point of such a model was the analytical computation of the inviscid flow around the projectile, which includes shocks and expansion waves but no reflection at the walls. From the numerical simulations of both inviscid flow and viscous flow inside the channel, the importance of the physical phenomena not captured in the simplified analytical model is determined. Corrective factors are then introduced into the analytical model to account for:

28

- reflections on the wall;
- interactions between shocks and expansion waves;
- viscous effect, such as development of a boundary layer on the projectile and sock-boundary layer interactions.

These correction factors will be applied to the drag, lift, and moment coefficients, and will be functions of the Mach number, gap size between the projectile and the channel walls, and projectile angle of attack.

Figure 18 through Figure 24 show the velocity, pressure, and temperature fields inside the channel. Inviscid cases are presented in Figure 18 through Figure 20 and Figure 25, while viscous results can be seen in
Figure 21 through Figure 24.
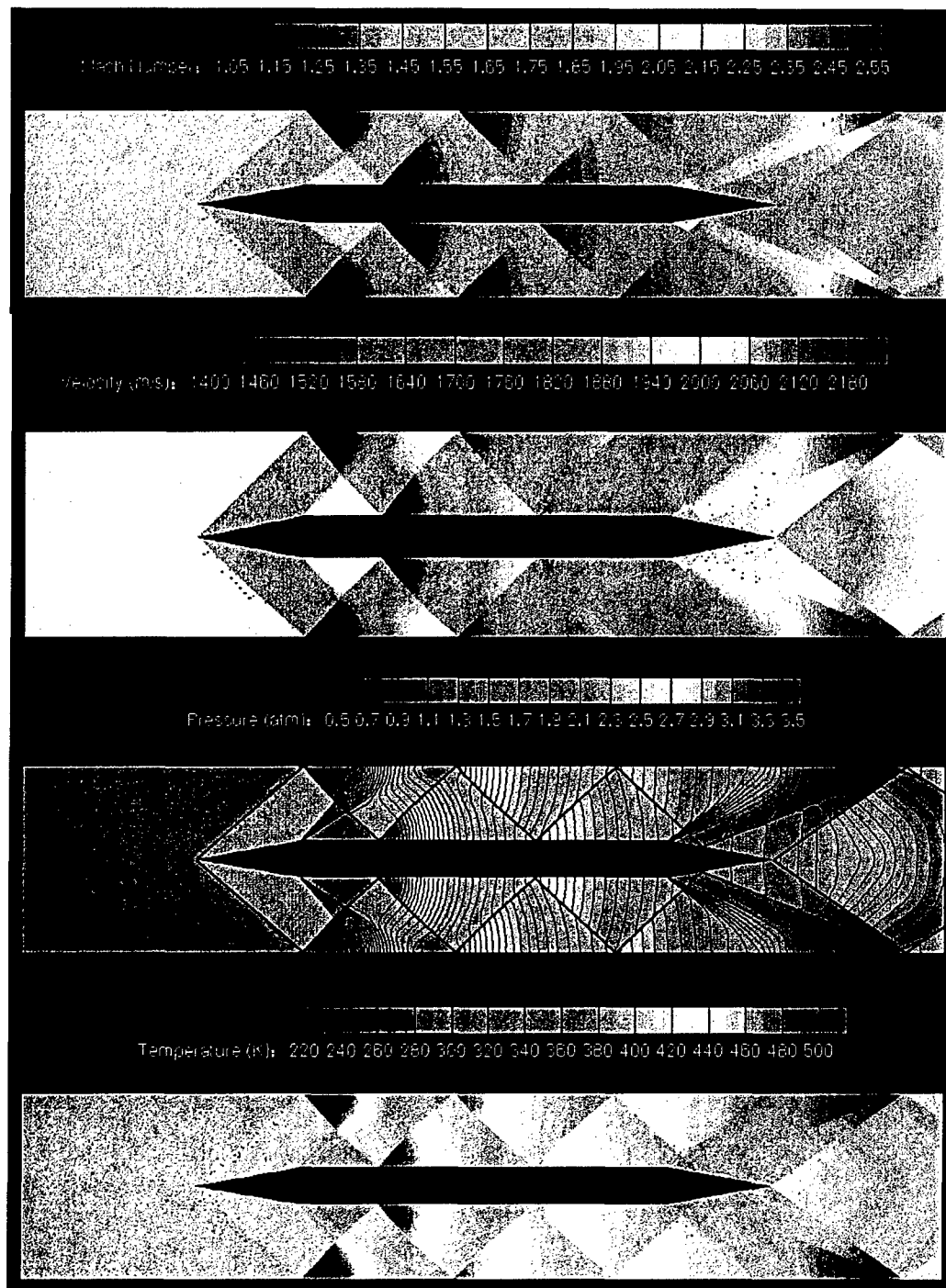
Figure 18: Projectile traveling at Mach 2 through inviscid helium at 1 atm.
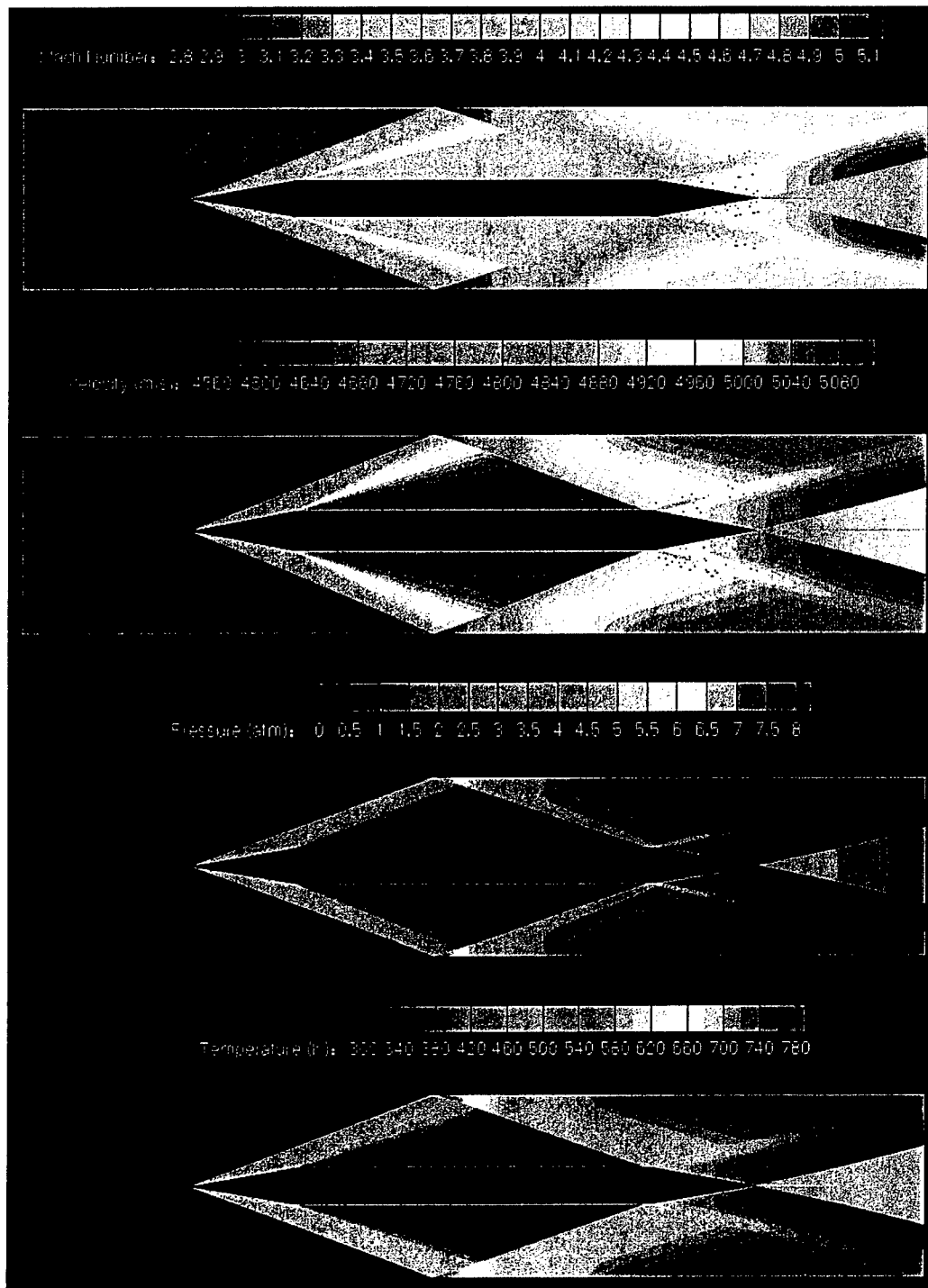
Figure 19: Projectile traveling at Mach 5 through inviscid helium at 1atm.
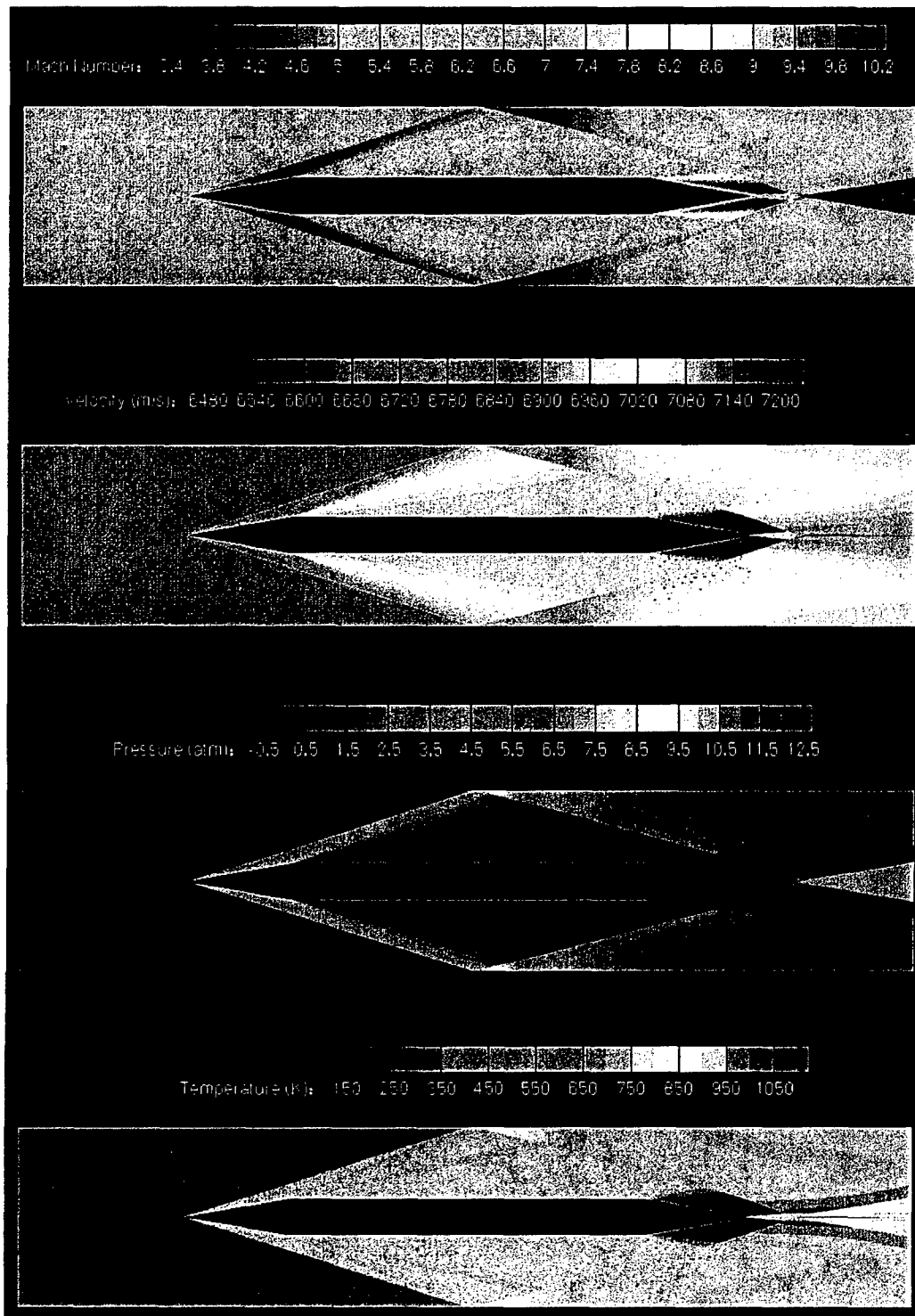
Figure 20: Projectile traveling at Mach 7 through inviscid helium at 1atm.
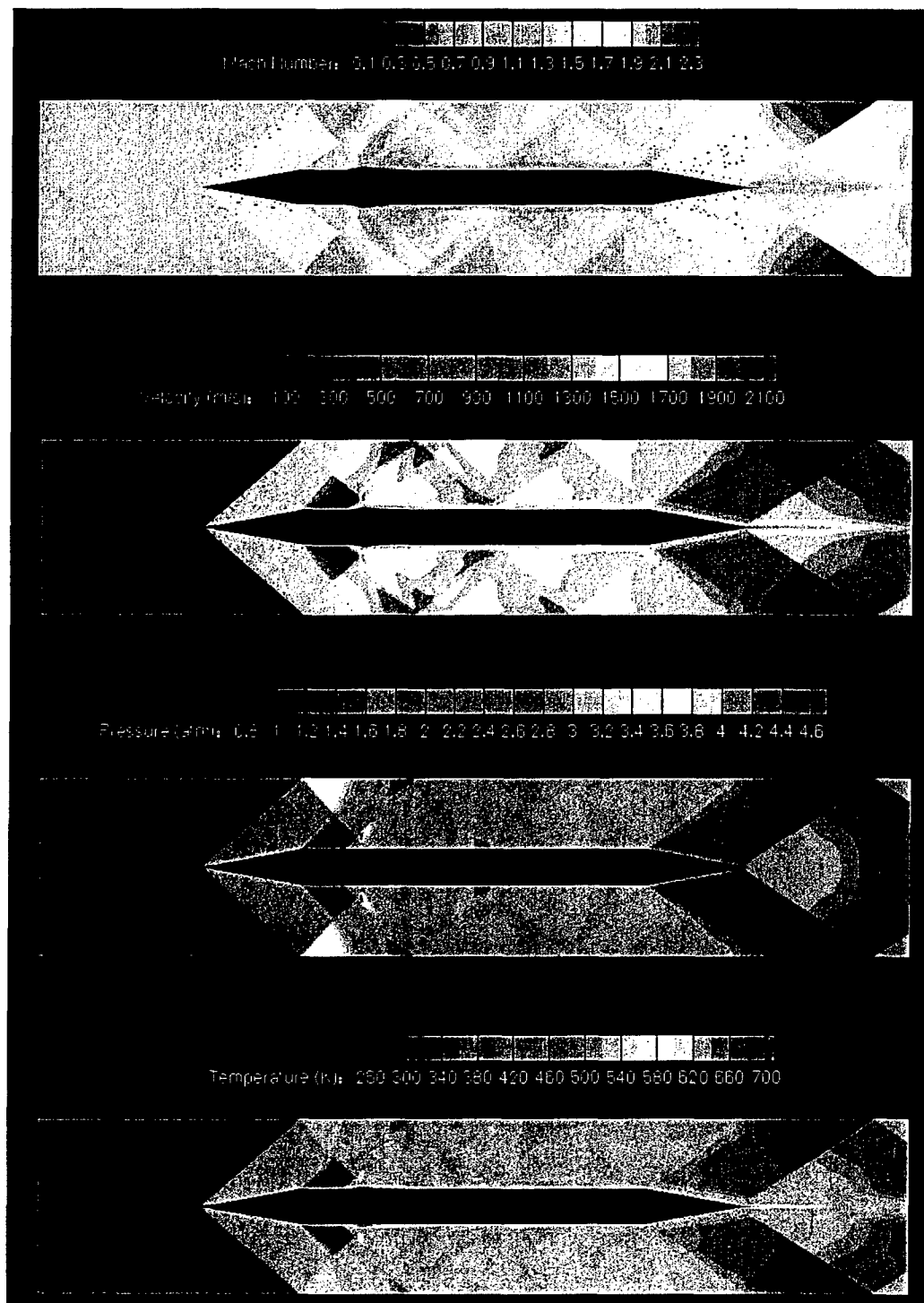
Figure 21: Projectile traveling at Mach 2 through viscous helium at 1atm.
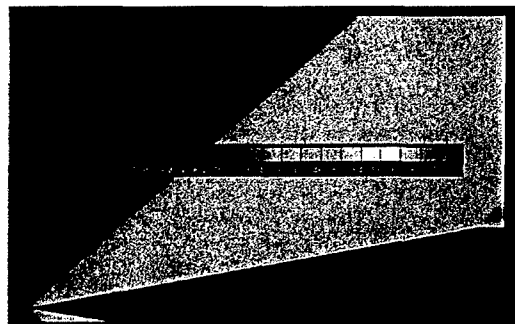
33

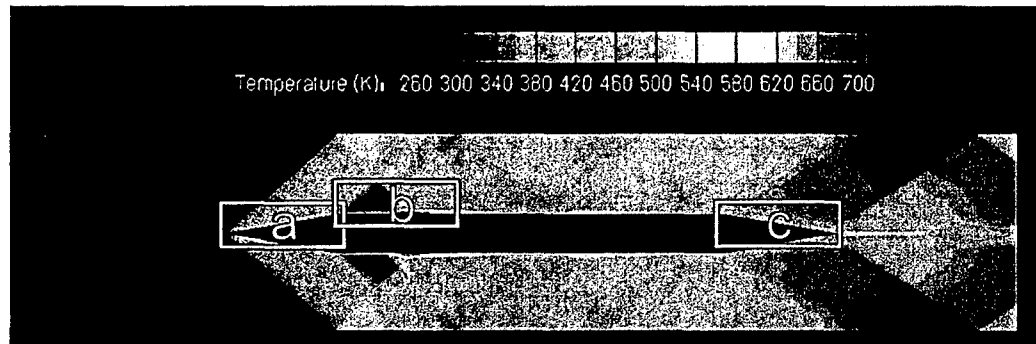**(a)** Closer view of the leading edge   **(b)** Bloser view of trailing edge
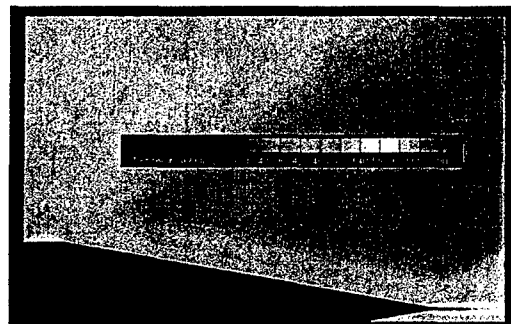
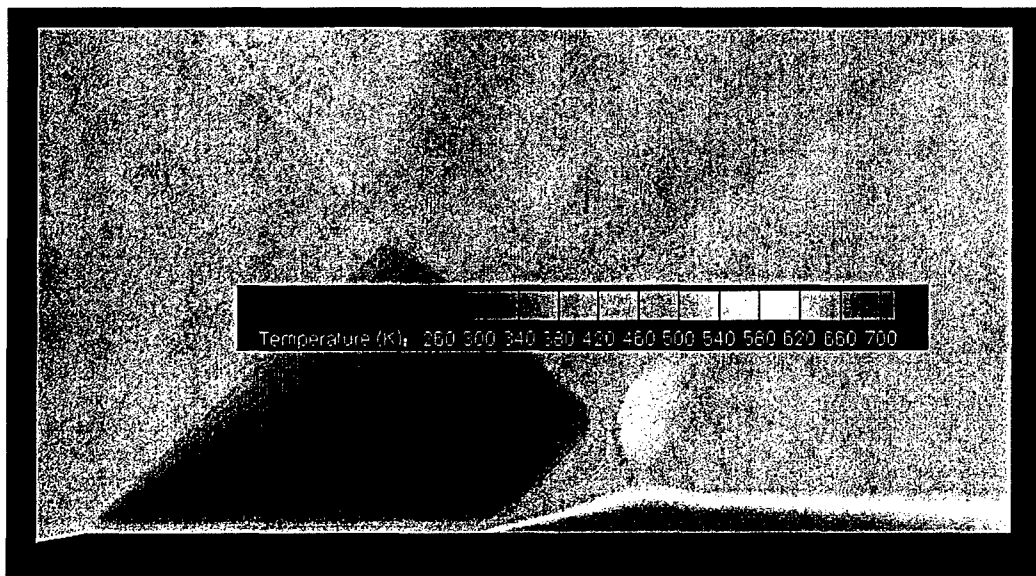**(c)** Closer view of the shock-boundary layer interaction

Figure 22: Closer view on the velocity field around a projectile traveling at Mach 7 through inviscid helium at 1atm.
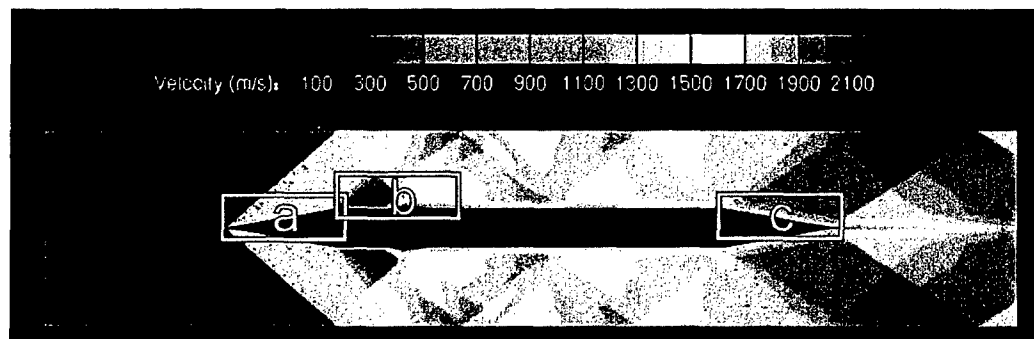
(a) Closer view of the leading edge   (b) Closer view of trailing edge

(c) Closer view of the shock-boundary layer interaction

Figure 23: Closer view on the temperature field around a projectile traveling at Mach 7 through inviscid helium at 1atm.
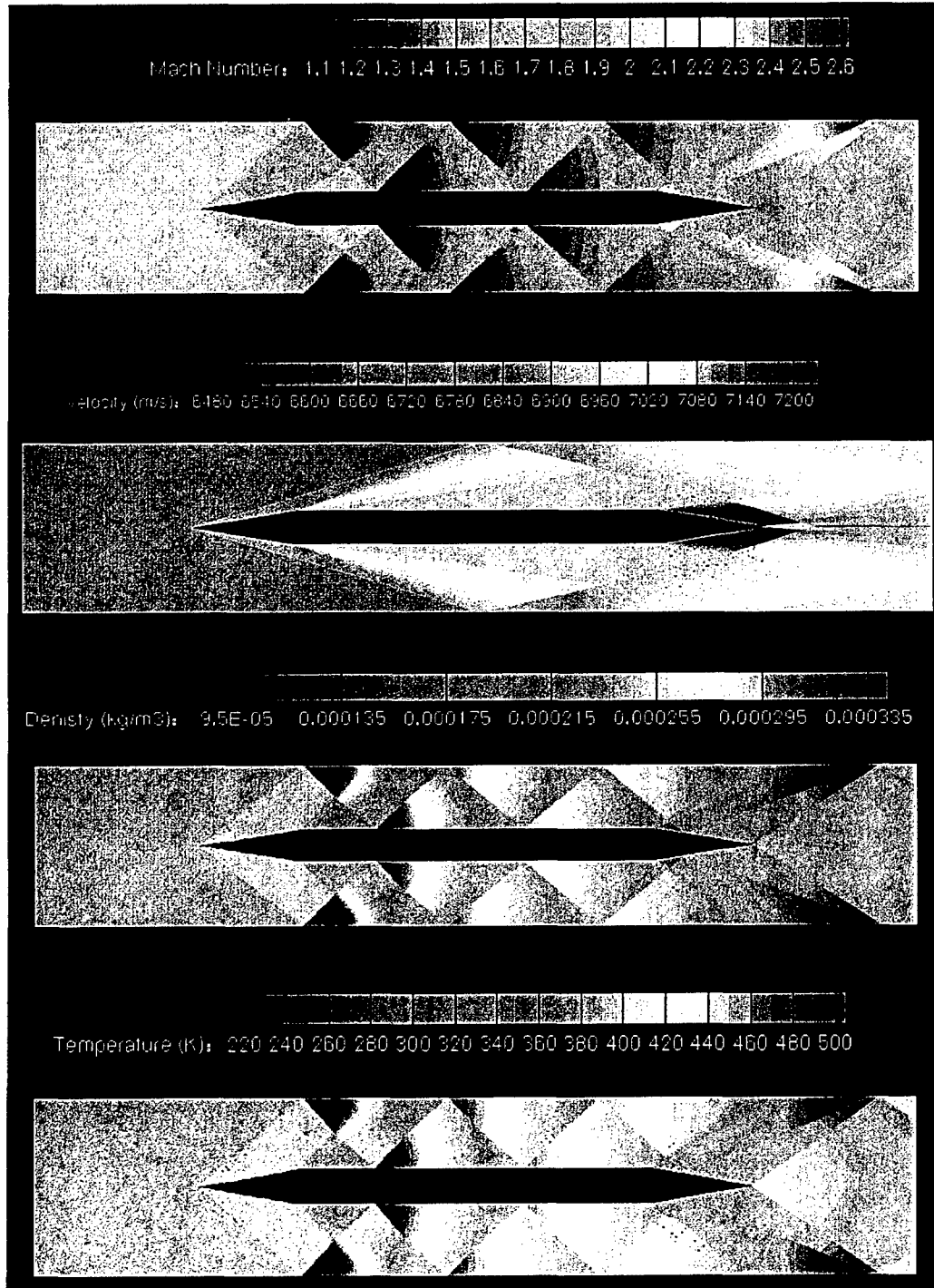
35

Figure 24: Projectile traveling at Mach 7 through inviscid helium at 0.001 atm.

As can be seen in Figure 23 (a), the boundary layer on the projectile is very thin at such high speeds because the flow carries a lot of inertia. Figure 23 (c) shows the thin wake being shed off the back of the projectile. When a shock is reflected by the projectile wall, it interacts with the boundary layer and causes boundary layer separation as illustrated in Figure 23 (b).

In the viscous flow at Mach 2 of Figure 24 (a), one can see a significant increase in temperature close to the walls caused by the fluid viscosity which dissipates the fluid energy as heat. Figure 24 (b) shows the high-temperature flow being carried away by the wake. Moreover, the highest temperatures on the sled are linked to viscous heating at a shock-boundary layer interaction, as can be seen in Figure 24 (c).

The comparison of the inviscid and viscous cases simulated shows that the viscous effects increase the drag coefficient of the projectile by between 10% and 15%. For instance the drag coefficient is 0.00736 when the projectile is traveling at Mach 2 in inviscid helium at 1 atm and it is 12% higher when the flow is viscous. At Mach 5, the drag coefficient increases by 10% due to the fluid viscosity.

Table 3: Comparison of drag force per unit span and drag coefficient for inviscid and viscous simulations at different speeds. Percents are with respect to the inviscid case at 1atm.

Case	Drag Per Unit Span	Drag Coefficient	
Inviscid 1atm			
Mach 2	99 N/m	7.36×10^{-3}	
Mach 5	272 N/m	3.24×10^{-3}	
Mach 7	681 N/m	4.13×10^{-3}	
Viscous 1atm			
Mach 2	111 N/m	8.25×10^{-3}	(+12%)
Mach 5	302 N/m	3.59×10^{-3}	(+10%)
Mach 7	770 N/m	4.67×10^{-3}	(+13%)
Inviscid 0.001atm			
Mach 2	0.0996 N/m	7.40×10^{-6}	
Mach 5	0.277 N/m	3.20×10^{-6}	
Mach 7	0.692 N/m	4.20×10^{-6}	

It is interesting to note that the contribution of the shear drag to the total drag on the projectile is very small at such high Reynolds numbers with a projectile that generates only a very thin wake. If the channel were wider and the shocks were not to bounce back on the projectile, the viscous effects could certainly be neglected. However, the viscous effects are quite significant in our problem. Because of the presence of the boundary layer, the reflection on the projectile walls of a shock is radically altered. Hence the whole shock pattern depends strongly on viscous effects at the walls, and so does the net aerodynamic and aerothermal forces on the projectile.

Although the aerodynamic heating within the launch tube does not present a significant challenge (due to the low pressure and density of the gas) the heating of the projectile upon exit of the launcher into the dense ground-level atmosphere is an issue that must be thoroughly examined before a definitive statement on the feasibility of direct launch from the surface of the Earth to orbit can be made. For example, the projectile must be able to tolerate extremely large heat fluxes for 10-15 seconds as the projectile travels at around 7 km/s through the dense lower atmosphere. Numerous studies have indicated that flyout velocities of around 6.5 km/s are feasible from a heat transfer perspective, [1, 2]. Furthermore, these references indicate that at these speeds, "Sea level launch poses no unusual difficulty", [1]. Although these sources indicate that such launch speeds are feasible, experimental validation, especially using ablative techniques, has not been performed. Therefore, immediate work has begun on exploring appropriate analytical, numerical, and experimental techniques for assessing the performance of the projectile as it travels through the dense portion of the atmosphere at extremely high speeds and experiences heat fluxes on the order of several ten kW/cm^2, and a significant part of the Phase-2 effort will be dedicated to optimizing the shape of the projectile, examining various surface ablator materials (such as plasma sprayed tungsten which has recently been perfected), and the use of novel multi-layer aerodynamic shells to withstand the high heat loads. Numerical efforts will be explored to compliment the work currently being pursued by the University of Minnesota and the University of New Orleans.

To prepare for the Phase II effort in understanding what types of protective and/or ablative coatings are necessary to protect the projectile, it is first essential to model what type of heat loads the projectile will actually see during its flight through the atmosphere. To study this issue, a model was developed for both direct orbital insertion and flight of kinetic energy projectiles to determine what heat loads are expected as a function of both altitude and time. The following summarizes the model:

- As from the nomenclature used in Palmer&Dabiri[2], R_B is the base radius of the conical projectile and R_N the nosetip radius.
- The heat flux is computed from Palmer&Dabiri equation (1), and is assumed to be maximal at the time of launch since the ratio of atmospheric densities at altitude h and launch altitude ρ_h/ρ_0 are then maximal. Thus, for a launch speed V, the maximum heat flux is taken to be

$$\frac{1}{A}\frac{dQ}{dt}\bigg|_{max} \approx 3.4 \times 10^{-4}(R_N)^{-0.2}V^{3.18}\left(\frac{\rho_h}{\rho_0}\right)^{0.8}.$$

- The launch velocity, V, is set so that the maximum heat flux is 280 MW/m^2.
- The drag coefficient, C_D, is assumed to be only a function of the cone angle, θ_c, and the ratio of nosetip radius to base radius, according to Palmer&Dabiri equation (3), namely

$$C_D = 2\sin^2\theta_c + \left(\frac{R_N}{R_B}\right)^2\left(1 - 2\sin^2\theta_c - \sin^4\theta_c\right)$$

---

[2] M.R. Palmer and A.E. Dabiri, "Electromagnetic space launch: a re-evaluation in light of current technology and launch needs and feasibility of a near term demonstration", *IEEE Transactions on Magnetics*, Vol. 25, No. 1, January 1989.

- The cone angle, θ_c, is 4°.
- The launch angle is taken to be the one for which the projectile has no vertical velocity when reaching LEO altitude (180km or 300km).
- Launch takes place due East from Kennedy Space Center.
- The speed required for circularization at LEO 180km is 7,802m/s.
- The speed required for circularization at LEO 300km is 7,732m/s.
- The density of the projectile is 3000 kg/m^3, as in Palmer&Dabiri.
- The mass of the projectile is determined from its volume and density.

The methodology and assumptions for these computations can be found in the paper by Uranga et al.[3] In particular, the circularization speed is given by

$$V_s = \sqrt{\frac{GM_E}{R_E + h}} = R_E \sqrt{\frac{g_0}{R_E + h}}$$

where $G = 6.67 \times 10^{-11}$m^3/kg/s^2 is the universal gravitational constant, $M_E = 5.97 \times 10^{24}$kg is the mass of the Earth, $R_E = 6.380 \times 10^6$m is the radius of the Earth, h is the orbital altitude above the Earth's surface in meters, and $g_0 = 9.81$m/s^2 is the acceleration due to gravity on the Earth's surface.

For any base radius, the curves in **Figure 25** and **Figure 26** have a maximum, meaning that there is a ratio of radii, R_B/R_N, that will maximize the horizontal velocity at LEO altitude. In other words, for a given projectile base radius R_B (so for a given projectile volume and hence payload size), there is an optimal nosetip radius R_N that will maximize the speed at orbital altitude while keeping the heat flux below a set value (280 MW/m^2 here). A summary of geometry and launch parameters for launch to orbits of 185 and 300 km are summarized in Tables 2 and 3.

[3] A. Uranga, D. Kirk, H. Gutierrez, R. Meinke, and K. Barker, "Rocket performance analysis using electrodynamic launch assist", *Proceedings of the 43rd AIAA Aerospace Sciences Meeting and Exhibit*, Paper No. AIAA-2005-1449, Reno, Nevada, Jan. 10-13, 2005.

Table 4: Unpowered projectile to LEO (300 km).

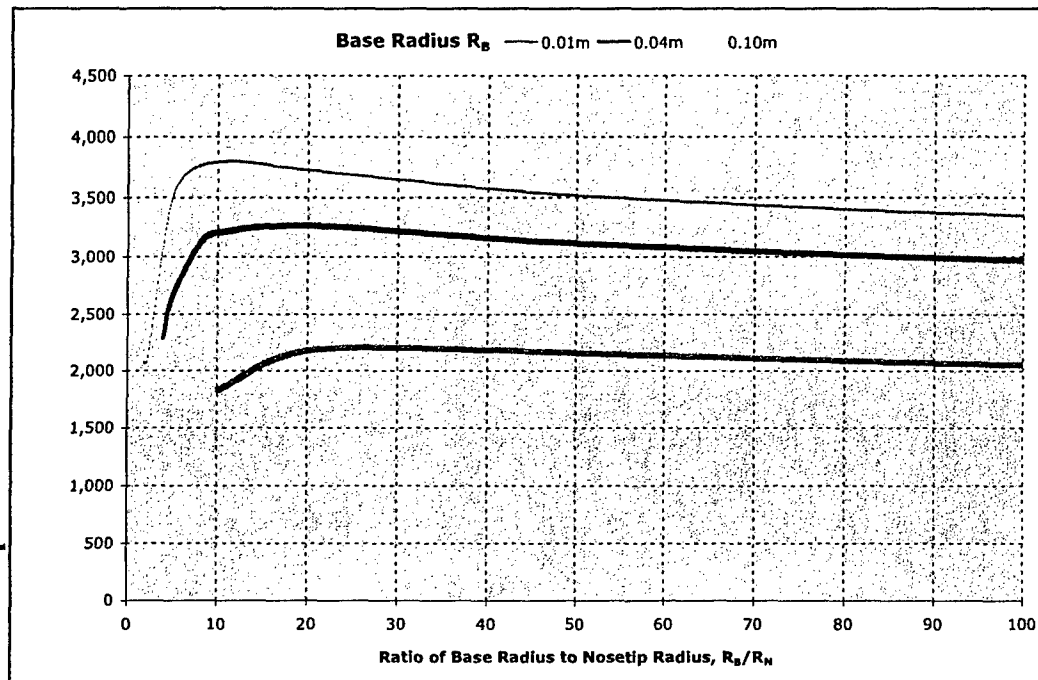| R_B (m)	Mass (kg)	R_N (m)	R_B/R_N	Launch Mach Number for 280 MW/m^2	Launch Angle (°)	Horizontal Velocity at h_{LEO} (m/s)
0.01	0.090	0.0001	100	9.197	65.9	1,465
		0.000125	80	9.328	64.5	1,535
		0.0002	50	9.607	62.2	1,654
		0.00025	40	9.743	61.3	1,701
		0.0005	20	10.177	60.7	1,732
		0.001	10	10.631	70.1	1,260
0.04	5.758	0.0004	100	10.036	47.4	2,587
		0.0005	80	10.177	46.6	2,649
		0.0008	50	10.483	45.1	2,772
		0.001	40	10.631	44.4	2,829
		0.002	20	11.105	42.8	2,969
		0.004	10	11.599	42.9	2,953
		0.005	8	11.763	43.9	2,863
		0.008	5	12.116	49.6	2,414
		0.01	4	12.287	55.7	2,014
0.10	89.963	0.001	100	10.631	42.3	3,016
		0.00125	80	10.781	41.6	3,080
		0.002	50	11.105	40.2	3,215
		0.0025	40	11.261	39.6	3,277
		0.005	20	11.763	37.9	3,457
		0.01	10	12.287	36.9	3,563
		0.02	5	12.835	38.6	3,375
		0.05	2	13.596	59.4	1,797

Figure 25: Horizontal projectile velocity when reaching LEO (180 km) versus ratio of base to nosetip radii.
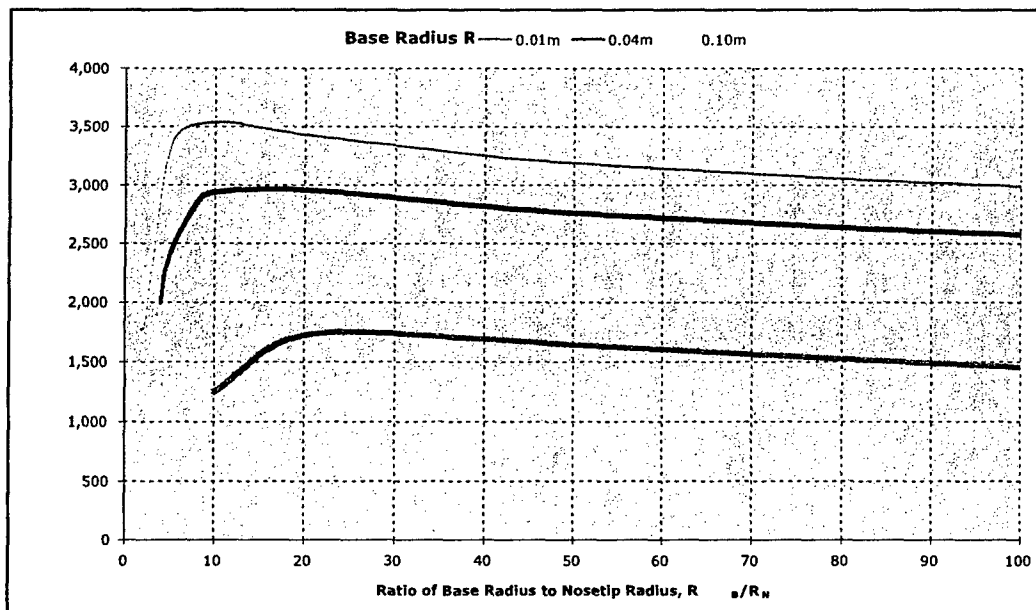

Figure 26: Horizontal projectile velocity when reaching LEO (300 km) versus ratio of base to nosetip radii.

The model also calculates optimized projectile geometry for a given base radius and desired altitude (or range) for minimization of heat flux. This is in contrast to most models which attempt to minimize the initial muzzle velocity. In other words, the model helps selecting the best geometry for smallest heat load to the projectile for a given mission.

It seems feasible to utilize experimental methods to investigate the high heat fluxes originated by atmospheric coasting from ground by making use of electron beam welding techniques, which can produce surface heat fluxes as high as 10^3-10^6 kW/cm^2, [5]. Although the actual physical situation between shear layer heating during atmospheric flight and electron beam penetration to achieve the heat flux is quite different, exposing various nose cone geometries or cooling techniques to these intense heat loads will nonetheless provide valuable guidance for the design of the actual projectile.

If the projectile can withstand the high heat loads during the initial ascent (first several seconds), the heat flux then monotonically decreases to much more tolerable levels (2-5 kW/cm^2). Current research suggests that, *"Lightweight flexible phenolics, such as PhenCarb-28 at 28 lb/ft^3, look promising for [planetary exploration] missions with peak heating in the range from about 1,000 to 2,000 Btu/ft^2-sec (~1.1 to 2.3 kW/cm^2). A Phencarb-32 or -36 should have more optimal performance and efficiency for still higher heating"*, [5]. The existing arc-heated facility -NASA MSFC PRL- is capable of producing heat fluxes on the order of 0.5 kW/cm^2, so heat transfer experiments simulating the projectile at times after flight through the densest portions of the atmosphere (after the first 1-5 seconds) can be readily accomplished.

Another option includes plasma sprayed high-temperature refractory metals and ceramics. For example, *"Ultramet has developed and repeatedly demonstrated a refractory ceramic coating material capable of non-ablating, long-term operation (minutes to tens of minutes) under air arcjet conditions at heat flux and enthalpy levels, simulating leading edge reentry conditions, of 350 Btu/ft^{2}sec (~0.4 kW/cm^2) and 12,000 Btu/lbm respectively. This unique material has also survived heat flux levels as high as 800 Btu/ft^{2}sec (~1 kW/cm^2), without erosion, under lower enthalpy conditions. This patented coating material, designated Ultra2000, is composed of fine alternating layers of hafnium carbide (HfC) and silicon carbide (SiC), applied by chemical vapor deposition (CVD), to a total thickness of just 0.005-0.010". Ultra2000 is capable of long-term, non-ablating operation at surface temperatures as high as 4000°F, and has been effectively applied to and tested on various ceramic matrix composites, carbon-carbon composites, and graphite substrates"*, [5].

In summary, it appears that if the projectile can survive the intense heat fluxes for the first few seconds of launch (1-3 seconds to arrive at 16,000 km, where the atmospheric density has already dropped significantly), proven thermal protection systems are then available to protect the projectile for the remainder of the flight. The Phase-2 contract will explore each of these options, and use appropriate teaming (Ultramet, Plasma Processes, Inc., etc.) to develop and test an appropriate thermal protection system.

7. Combined Simulation of Electromagnetic and Aerodynamic Forces

An integrated simulation tool that combines the electromagnetic and aerodynamic forces acting on the projectile is currently being developed to calculate the multi-DOF projectile trajectory during acceleration. The simulation consists of the following sub-modules:

1. Computation of the instantaneous electromagnetic forces and torques induced in the projectile by the currently active track coils (on Figure 1, T_{RI} and T_{FI}). In the example's rear section, these depend on the currents i_{RI}, i_{FI}, the local axial position x, and the geometric relationships between track and projectile.

This module consists of the following sub-modules:

1.1 Computation of the instantaneous mutual inductance between the projectile coils and the corresponding track coils. In the example this means T_{RI} with P_R and T_{FI} with P_F. Inputs to this sub-module are:

- The coils' radii (R_p and R_t for projectile and track, respectively).

- The $<x,y,z>$ vector of relative position between coil centers ($x=$ distance between coils' centers along the launch axis, $y=$ horizontal distance, $z=$ vertical distance).

- The pitch (θ_y) and yaw (θ_z) angles of both projectile's coils relative to the local coordinate system X fixed on the corresponding track coil.

Single turn coils represented by infinitely thin filaments will be considered first. Later, approximate 3D coil geometry (coil thickness and depth) will be included.

1.2 Computation of the instantaneous electromagnetic propulsion, lift and guidance forces acting on the projectile. This sub-module consists of:

- Evaluation of the gradient of the mutual inductance calculated in Module 1.1 for the current $<x,y,z>$ vector of relative position between coil centers.

- Computation of the $<F_x,F_y,F_z>$ vector of electromagnetic forces acting on both front and rear projectile coils. This is based on the mutual inductance gradient calculated above and the corresponding instantaneous currents (i_{RI} with i_{PR}, i_{FI} with i_{PF}).

1.3 Computation of electromagnetic torques acting on the projectile. The forces calculated on Module 1.1 will be used to calculate the electromagnetic torques created by the propulsion, guidance and lift forces.

2. Computation of the instantaneous aerodynamic forces and torques induced in the projectile during launch. This module consists of the following sub-modules:

2.1 Computation of the 3D aerodynamic forces created by the pressure distributions acting on the projectile's surface, as a result of the reflection of shock waves within the launch tube. A simplified model of the pressure distributions, validated by computational fluid dynamics state-of-the-art software, will be used.

2.2 Computation of aerodynamic torques acting on the projectile as a result of the forces calculated in Module 2.1.

43

3. Computation of the 6-DOF trajectory of the projectile during launch. This module consists of:

- The electromagnetic and aerodynamic forces and torques calculated by Modules 1.2, 1.3, 2.1 and 2.2 are used to estimate the multi-DOF projectile trajectory (based on integration of Newton's equations of motion) in a sub-section of the track such as the shaded area on Figure 9.

- An algorithm that connects the motion in the present sub-section of the track with the next sub-section.

The integrated simulation will be a novel and valuable tool. It will be used:

- To prove the feasibility and design requirements of the CFSM launcher concept.

- To develop design optimization of the launcher geometric parameters.

- To provide insight in the interaction of electromagnetic and aerodynamic effects during launch.

During Phase-2, the launcher simulation will be integrated with mathematical models of the energy sources, switching devices and other power electronics. This will allow:

- To estimate the performance of the CFSM concept in a full-scale design.

- To optimize parameters of the power conversion system.

- To study the need and/or feasibility of a real-time feedback system to optimize the performance of the CFSM system.

8. Experimental Qualification of the CFSM Concept

The constant-flux principle is based on the static relationships of current-field-flux given by the geometric relationships between track coils and projectile coils. Therefore the principle can be tested under semi-static conditions (low speed). Figure 5 shows a section of a test set-up used to demonstrate the constant-flux principle.
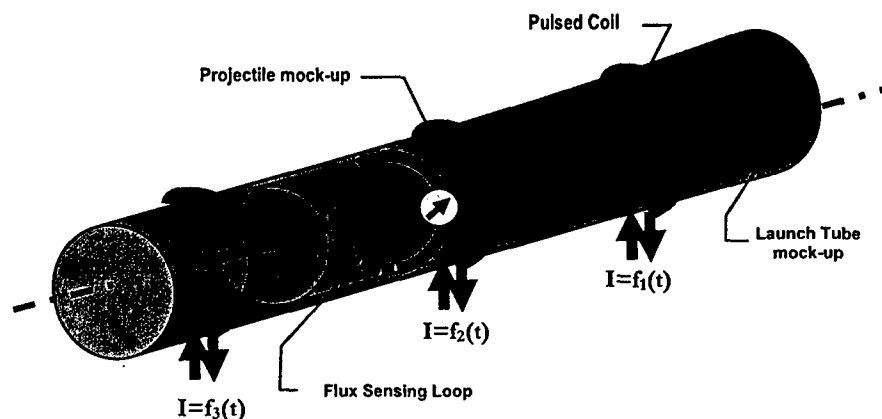

Figure 27: Linear test rig for qualification tests of the CFSM system.

The linear test rig represents a section of the launch tube with a few track coils implemented. A projectile mock-up will be moved along the tube to trigger the sequence of current pulses $f_1(t)$, $f_2(t)$, $f_3(t)$. The mock-up projectile is rigged with a flux sensing coil - any flux change experienced by the test coil would induce a voltage that can be externally measured. Integrating the signals from the flux sensing loops measures the total flux change seen by the test coil. The projectile mock-up can be moved to any position relative to the pulsed track coils, and the current waveforms calculated by solving (11) subject to (12) can be generated by computer-controlled current sources. Applying the calculated pulse shapes to the mock-up track coils and measuring the induced voltage simulates the flux seen by the coil on the moving projectile. Flux measurements as a function of time will be performed for all positions between two track coils. For a correctly shaped current pulse, the measured voltage and therefore the flux should be constant at all test positions.

The tests will show what level of accuracy in pulse-shaping is needed to experience acceptable flux changes in the actual system, or otherwise, which flux changes will be seen by the moving projectile coils for a given inaccuracy in the actual pulse shape. These tests and the corresponding calculations will help optimize the CFSM system, and estimate the induced voltages (and therefore parasitic currents) induced in the moving projectile as a result of non-ideal pulse shaping. While it is in principle possible to adjust the pulse shapes to any level of accuracy, system complexity, robustness and cost suggests the use of the simplest pulse power system that will not cause quenching and overheating of the projectile coils. Various coil configurations for track and projectile can be tested and compared with calculations. The linear test rig could also be used to measure the propulsion and levitation forces, using active coils in the projectile mock up. Since the mock-up would only move over short distances, external connections for the coils would be easy to implement.

45

8.1 Superconductor Qualification Tests

Quench Stability

A prototype coil consisting of a few turns of superconductor would be excited to the required operational current. A second coil in close proximity would be used to simulate the flux changes that are expected in actual operation of these coils. Inducing flux changes of various levels into the prototype projectile coil, its quench stability can be tested. The flux changes used in these tests can be stronger than expected in the actual system to guarantee a sufficient operational margin during actual operation.

Mechanical Stability

During launch, the superconductor in the projectile coil will experience significant mechanical forces due to inertial acceleration. Superconductors (either LTS or HTS) have never been tested under such conditions. The inertial acceleration is equivalent to compression of the conductor, i.e., the mechanical launch conditions can be simulated by compressing the conductor. To test stability to mechanical stress, the conductor would be placed in a cryostat with a background field of appropriate strength that simulates the self-field of the projectile coil and the field due to the track pulses. The conductor is then loaded to the appropriate mechanical pressure and its critical current measured. The conductor and its enclosure should pass these tests without quench with at a significant safety margin. These tests can be performed with different superconductors to identify the best choice.

8.2 Study of Nose Cone Ablation

As already presented in Section 6, the coasting flight of the projectile through the atmosphere remains a major issue and requires special testing. High intensity particle beams, as used on electron beam welding, produce sufficient heat flow densities to simulate the effects of low-altitude atmospheric coasting on the projectile.

It seems feasible to use experimental methods to investigate the high heat fluxes originated by atmospheric coasting from ground by making use of electron beam welding techniques, which can produce surface heat fluxes as high as 10^3-10^6 kW/cm^2 [3]. Electron beams used for welding are of rather lower energy, and the particles are absorbed in thin layer of the irradiated object. However, the drag form the atmosphere, which might quasi peel off the heated layer would be difficult or impossible to simulate in such experiments. Spinning the irradiated object might be a possibility to simulate such a peel-off effect from the atmosphere. Although the actual physical situation between shear layer heating during atmospheric flight and electron beam penetration to achieve the heat flux is quite different, exposing various nose cone geometries or cooling techniques to these intense heat loads will nonetheless provide valuable guidance for the design of the actual projectile.

46

9. System Integration

A conceptual design of a complete electromagnetic launch system for affordable, agile access to space consisting of a approximately 500-m long track with a inclination of about 45 degrees, the required propulsion system, the reduced-pressure helium atmosphere in the launch tube has been performed during Phase-1 and is described in previous and the current Status reports.

The tests described in section 4 of this report will enable us to perform a more detailed design of the system during Phase-2. This design will also include the required pulse power system and the energy storage system, and a concept for the low pressure launch tube. Since large forces will be experienced by the track coils of the CFSM system, a concept for supporting these will be presented. The track support concept has to include requirements for the alignment of the launch tube. Special attention has to be given to the fact that the launch tube has to consist of a non-conductive material, most likely a fiber-reinforced composite.

9.1 Scalability

The proposed launch system concept has great potential for scalability. Although our design studies focused on a projectile mass of about 100 kg, consisting of a launch vehicle with a mass of 5-10 kg and a roughly 10 times larger support structure with superconducting coils in their cryostat and the nose and rear cones (material of cones is TBD, see section 4.1 and 4.2) of the projectile, it seems possible to design similar systems with different parameters. Based on the work performed so far, it seems possible to increase the projectile mass within realistic limits, in particular, if the requirements for acceleration (currently 5000 gee) and/or the required launch velocity (currently 7000 m/sec) are reduced. Such variations of design parameters should open up possibilities for various other applications of the system.

10. References

[1] Palmer, M. R., Dabiri, A. E., "Electromagnetic Space Launch: A Re-Evaluation in Light of Current Technology and Launch Needs and Feasibility of a Near Term Demonstration," *IEEE Transactions on Magnetics*, Vol. 25, No. 1, January 1989.

[2] Rice, E. E., Miller, L. A., Earhart, R. W., "Final Technical Report on Preliminary Feasibility Assessment for Earth-To-Space Electromagnetic Railgun Launchers," NASA Final Technical Report NAS3-22882, June 30, 1982.

[3] Dave, V. R, Goodman, D. L., Eager, T. W., Russell, K. C., "High Energy Electron Beam Welding and Materials Processing."

[4] http://www.inspacepropulsion.com/nra3.html

[5] http://www.ultramet.com/u2000tps.htm

[6] McNab, I. R.: "Launch to Space With an Electromagnetic Railgun," *IEEE Transactions on Magnetics*, Vol.39, No.1, Jan 2003.

[7] J. de Boeij, M. Steinbuch and H. Gutiérrez: "Modelling the Electromechanical Interactions in a Null-Flux EDS Maglev System," *IEEE Transactions on Magnetics*, Vol.41, No.1, Jan 2005.

[8] J. de Boeij, M. Steinbuch and H. Gutiérrez: "Mathematical Model of the 5-DOF Sled Dynamics of an Electrodynamic Maglev System with a Passive Sled," *IEEE Trans. on Magnetics*, Vol.41, No.1, Jan 2005.

[9] E. R. Laithwaite: "Induction coil guns for hypervelocities," *IEE Proceedings in Electric Power Applications*, Vol. 142, No. 3, May 1995.

[10] E. R. Laithwaite, "Adapting a linear induction motor for the acceleration of large masses to high velocities," *IEE Proceedings in Electric Power Applications*, Vol. 142, No. 4, J u l y 1995.

[11] R. J. Kaye, E. L. Brawley, W. Duggin, E. C. Cnare, D. C. Rovang, M. M. Widner: "Design and Performance of a multi-stage cylindrical reconnection launcher," *IEEE Trans. on Magnetics*, Vol. 27, No. 1, Jan 1991.

[12] M. Cowan: "A Momentum Limit for Electromagnetic Railguns," *IEEE Transactions on Magnetics*, Vol. 29, No. 1, Jan 1993.

[13] R. J. Kaye: "Operational Requirements and Issues for Coilgun Electromagnetic Launchers." *IEEE Transactions on Magnetics*, Vol. 41, No. 1, Jan 2005.

[14] R. J. Thome and J. M. Tarrh: MHD and Fusion Magnets, Field and Force Design Concepts.

[15] K. Ki-Bong, E. Levi, Z. Zabar, L. Birenbaum: "Mutual Inductance of Noncoaxial Circular Coils with Constant Current Density," *IEEE Transaction on Magnetics*, Vol 33, no. 5, Sept 1997.

[16] B. Marder: The Physics of SERAPHIM. Sandia National Laboratory, Report No. SAND2001-2951, October 2001.

Estimate Electromagnetic Launch Assist

The program estimates key parameters for electromagnetic launch assist. The input parameters are defined in the following section (yellow fields). Physical units are used throughout the program and input and results can be given or displayed in any unit. Areas high-lighted in yellow are input. Areas high-lighted in green show conversions to other units or results.

MagLifter Input Parameters:

Launch assist speed (max) $v_e := 7000 \cdot \dfrac{m}{sec}$ $v_e = 15659 \dfrac{mi}{hr}$ $v_e = 20.35 \, Mach_{air}$ $v_e = 7 \, Mach_{helium}$

Acceleration (constant) $b := 5000 \cdot g$ $b = 4.9 \times 10^4 \, msec^{-2}$

Deceleration $d := 1000 \cdot g$ *Without a deceleration system the sled is lost after the launch!*

Projectile mass (GLOW) $M_{vehicle} := 5 \cdot kg$

Sled: Mass: $M_{sled} := 100 \cdot kg$ Drag coefficient: $C_{drag} := 0.1$ X-section area: $A := 0.5 \cdot m^2$

Total mass to accelerate including sled $M_{tot} := M_{vehicle} + M_{sled}$

Guideway/sled clearance (conservative) $gap := 2.5 \cdot cm$

Efficiency of linear motor $\varepsilon := 1.0$

Track slope angle $\alpha_{track} := 45 \cdot deg$

Acceleration Time

$$dT(v,b) := \frac{v}{b}$$

Acceleration time

$$dT(ve,b) = 0.14\,sec$$

Deceleration time

$$dT(ve,d) = 0.71\,sec$$

Without deceleration the sled is lost in each launch!

Track Length

$$s(b,t) := \frac{1}{2} \cdot b \cdot t^2$$

Acceleration length

$$sa := s(b, dT(ve,b)) \qquad sa = 499.66\,m \qquad sa = 1.64 \times 10^3\,ft$$

Decelaration length

$$sd := s(b, dT(ve,d)) \qquad sd = 1.25 \times 10^4\,m \qquad sd = 4.1 \times 10^4\,ft$$

Total Track length

$$stot := sa + sd \qquad stot = 1.3 \times 10^4\,m \qquad stot = 8.07\,mi$$

Total track height increase

$$s\_height := \sin(\alpha_{track}) \cdot sa \qquad s\_height = 353.31\,m$$

Forces

Force to overcome track slope

$$F_{slope} := M_{tot} \cdot g \cdot \sin(\alpha_{track}) \qquad F_{slope} = 0.73\,kN$$

$$F_{acc} := M_{tot} \cdot b \qquad F_{acc} = 5.15 \times 10^3\,kN$$

Total Force (acceleration + lift)

$$F_{tot} := F_{slope} + F_{acc} \qquad F_{tot} = 5.15 \times 10^3\,kN$$

Estimate total force including magnetic drag (~5 %)

$$F_{Acc} := 1.05 \cdot F_{tot} \qquad F_{Acc} = 5.41 \times 10^3\,kN$$

Aerodynamic Drag Force

Gas densities:

$$\rho_{air} := 1.28 \cdot \frac{kg}{m^3} \qquad\qquad \rho_{he} := 0.179 \cdot \frac{kg}{m^3}$$

Temperature [K] $T := 293$

Drag force as function of velocity

$$F_{drag}(v, A, \rho) := C_{drag} \cdot \left(\frac{1}{2} \cdot \rho \cdot v^2 \cdot A\right)$$

Drag force at end of track:
Since ve >> Mach-1, the drag increase can be neglected

$$F_{drag\_air} := F_{drag}(ve, A, \rho_{air}) \qquad F_{drag\_air} = 1.57\,MN$$

$$F_{drag\_he} := F_{drag}(ve, A, \rho_{he}) \qquad F_{drag\_he} = 0.22\,MN$$

Ratio of drag to acceleration force at maximum speed:

$$R_{air} := \frac{F_{drag}(ve, A, \rho_{air})}{F_{Acc}} \qquad R_{air} = 0.29$$

$$R_{he} := \frac{F_{drag}(ve, A, \rho_{he})}{F_{Acc}} \qquad R_{he} = 0.04$$

$$ve = 7 \times 10^3\,m\,sec^{-1}$$

Velocity range for plot

$$vel := 0 \cdot \frac{m}{sec}, 5 \cdot \frac{m}{sec} .. ve$$

Ratio of air drag to propulsion force
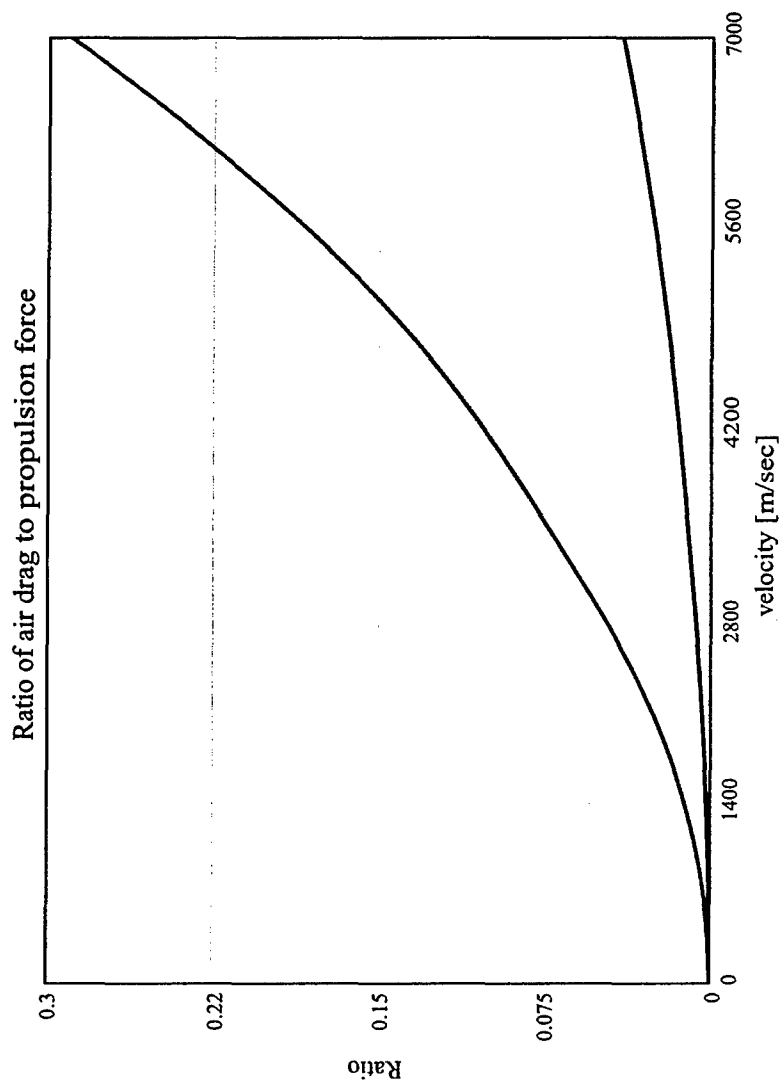
For high accelerations (b > 1400 g in air) the acceleration force dominates and the plotted ratio is less than 1. For smaller accelerations (b < 1400 g in air) the aerodynamic drag force dominates and the plotted ratio is greater than 1.

For helium the ratio of drag to propulsion falls below 1 for accelerations greater than 200 g.

Total forces (acceleration + air drag)
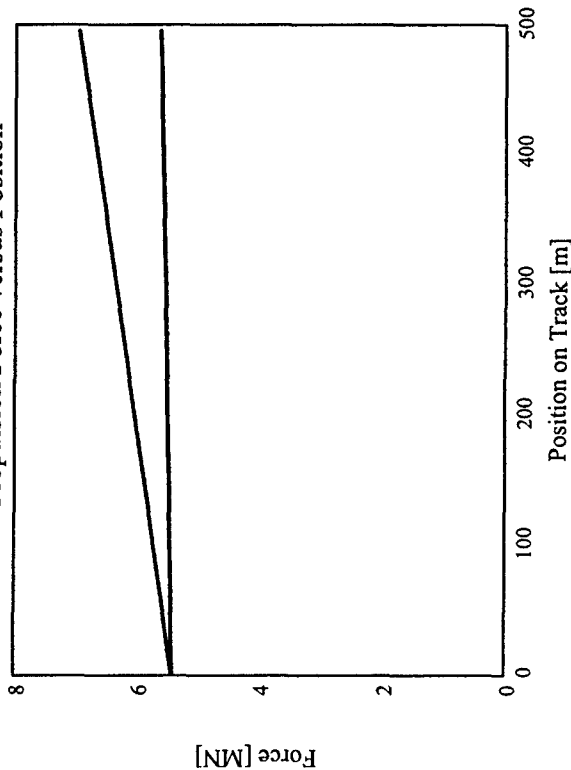
$$F_{Total\_air} := F_{Acc} + F_{drag\_air}$$

$$F_{Total\_he} := F_{Acc} + F_{drag\_he}$$

Total propulsion force versus position on track

For the design of the linear motor system it is necessary to know the total propulsion force, consisting of the contributions from acceleration, aerodynamic and electrodynamic drag.

$$F_{Prop}(s, A, \rho, T, \gamma) := \begin{vmatrix} \text{"Add air drag with drag increase and the acceleration force"} \\ \text{"Convert position 's' on the track to velocity"} \\ v \leftarrow \sqrt{2 \cdot b \cdot s} \\ F_{drag}(v, A, \rho) \cdot dragIncr(v, T, \gamma) + F_{Acc} \end{vmatrix}$$

$$ss := 0 \cdot m, 5 \cdot m .. sa$$

The dependence of propulsion force on position on the track is linear, because:.

$$v(s) = \sqrt{2 \cdot b \cdot s}$$

$$F_{drag} = C_{drag} \cdot \left(\frac{1}{2} \cdot \rho \cdot v^2 \cdot A \right)$$

red line: air
blue line: helium

The force of the linear motor system increases towards the end of the track. The increase is more pronounced for air than for helium.
The increase depends strongly on the selected acceleration. Very high accelerations require large acceleration forces and the aerodynamic drag is less important. For very large acceleration the aerodynamic drag becomes less important and the advantage of helium versus air is reduced.

Total Propulsion Force versus Position

Force [MN] versus Position on Track [m]

Energies

Energy to overcome track slope

$E_{lift} := M_{tot} \cdot g \cdot s\_height$ 　　　　$E_{lift} = 0.36\,Mjoule$

Energy to Lift Sled
Negligible compared to acceleration

$E_{levitation} := M_{tot} \cdot g \cdot gap$ 　　　　$E_{levitation} = 25.74\,joule$

Kinetic energy of sled at end of track

$E_{kin} := .5 \cdot M_{tot} \cdot ve^2$ 　　　　$E_{kin} = 2.57 \times 10^3\,Mjoule$

Get velocity as function of distance

$v = \sqrt{2 \cdot b \cdot s}$ 　　　Cross check: 　$\sqrt{2 \cdot b \cdot sa} = 7 \times 10^3\,m\,sec^{-1}$

Energy to overcome drag forces
Neglecting the drag increase near Mach 1

$$E_{drag\_air} := \int_0^{sa} F_{drag}\left(\sqrt{2 \cdot b \cdot x}, A, \rho_{air}\right) dx \qquad E_{drag\_air} = 391.73\,Mjoule$$

$$E_{drag\_he} := \int_0^{sa} F_{drag}\left(\sqrt{2 \cdot b \cdot x}, A, \rho_{he}\right) dx \qquad E_{drag\_he} = 54.78\,Mjoule$$

For comparison the energy is calculated
for helium, taking the drag increase near
Mach 1 into account. The drag increase
parametrization defined above for helium
is used.

$$EE_{drag\_he} := \int_0^{sa} F_{drag}\left(\sqrt{2 \cdot b \cdot x}, A, \rho_{he}\right) \cdot dragIncr\left(\sqrt{2 \cdot b \cdot x} \cdot \frac{sec}{m}, T, 1.67\right) dx$$

$$\frac{EE_{drag\_he}}{E_{drag\_he}} = 1.0011$$

For the end velocities of ve >> 500 m/sec that are of interest for
this project, the drag increase can be safely neglected (less than
1%). However for end velocites of ve ~ 500 m/sec the drag
increase boosts the necessary energy by more than a factor of 2.

Energy to overcome all forces (including efficiency)

$$E_{tot}(E_{drag}, E_{lift}, E_{kin}) := \frac{(E_{drag} + E_{lift} + E_{kin})}{\varepsilon}$$

$$E_{tot\_air} := E_{tot}(E_{drag\_air}, E_{kin}, E_{lift})$$

$$E_{tot\_he} := E_{tot}(E_{drag\_he}, E_{kin}, E_{lift})$$

$E_{tot\_air} = 2.96 \times 10^3 \, Mjoule$

$E_{tot\_he} = 2.63 \times 10^3 \, Mjoule$

Ratio of drag to kinetic energies:

$$\frac{E_{drag\_air}}{E_{kin} + E_{lift}} = 0.15$$

$$\frac{E_{drag\_he}}{E_{kin} + E_{lift}} = 0.02$$

Average power during acceleration

$dT(ve, b) = 0.14 \, sec$

$$P_{launch\_air} := \frac{E_{tot\_air}}{dT(ve, b)}$$

$$P_{launch\_he} := \frac{E_{tot\_he}}{dT(ve, b)}$$

$P_{launch\_air} = 20.77 \, Gwatt$

$P_{launch\_he} = 18.41 \, Gwatt$

Peak power:

$$P_{peak\_air} := (F_{drag}(ve, A, \rho_{air}) + F_{Acc}) \cdot ve$$

$$P_{peak\_he} := (F_{drag}(ve, A, \rho_{he}) + F_{Acc}) \cdot ve$$

$P_{peak\_air} = 48.82 \, Gwatt$

$P_{peak\_he} = 39.38 \, Gwatt$

Electricity cost for launch

$E_{tot\_air} = 823.5\,kW \cdot hr$

$E_{tot\_he} = 729.9\,kW \cdot hr$

$Cost\_air := E_{tot\_air} \cdot Cost\_kW\_hour$

$Cost\_he := E_{tot\_he} \cdot Cost\_kW\_hour$

$Cost\_air = 41.17\,dollar$

$Cost\_he = 36.5\,dollar$

Summary Page:

Input:

Launch assist speed:	$ve = 7 \times 10^3\,\mathrm{m\,sec}^{-1}$	Track slope angle: $\alpha_{track} = 45\,\mathrm{deg}$
Acceleration:	$b = 5 \times 10^3\,g$	Projectile mass (GLOW): $M_{vehicle} = 5\,\mathrm{kg}$
Sled: Mass: $M_{sled} = 100\,\mathrm{kg}$	X-section area: $A = 0.5\,\mathrm{m}^2$	Drag coefficient: $C_{drag} = 0.1$

Results:

Total mass to accelerate including sled:	$M_{tot} = 105\,\mathrm{kg}$
Track length for acceleration:	$sa = 499.66\,\mathrm{m}$
Acceleration force (without drag):	$F_{Acc} = 5.41 \times 10^3\,\mathrm{kN}$
Drag force (air, helium):	$F_{drag\_air} = 1.57 \times 10^3\,\mathrm{kN}$ $F_{drag\_he} = 219.28\,\mathrm{kN}$
Total propulsion force:	$F_{Total\_air} = 6.97\,\mathrm{MN}$ $F_{Total\_he} = 5.63\,\mathrm{MN}$
Kinetic energy:	$E_{kin} = 2.57 \times 10^3\,\mathrm{Mjoule}$
Drag energy (air, helium):	$E_{drag\_air} = 0.39\,\mathrm{Gjoule}$ $E_{drag\_he} = 0.05\,\mathrm{Gjoule}$
Total energy:	$E_{tot\_air} = 2.96\,\mathrm{Gjoule}$ $E_{tot\_he} = 2.63\,\mathrm{Gjoule}$
Peak power (air, helium):	$P_{peak\_air} = 48.82\,\mathrm{Gwatt}$ $P_{peak\_he} = 39.38\,\mathrm{Gwatt}$

Optimization of Acceleration Profile

The calculations above have shown that the forces necessary to accelerate the sled and the power are rising towards the end of the track. This effect is more pronounced for smaller accelerations, where the aerodynamic drag can be dominating the force requirements. Both paramenters constitute technological challenges for the realisation of the EMLA system. The requirements on the linear motor system and the energy storage system (concerning power) can be reduced by chooing an acceleration profil, which starts with a high acceleration and tapers off towards the end of the track. While the reduction of acceleration towards the end of the track, does not mitigate the aerodynamic drag forces, it still reduces the requirements on the linear motor and the energy strorage system.

To investigate the relevance of acceleration profile on the motor and power system requirements, the following profile is chosen (The parameter Δs has to be larger than the calculated track length SA !):

Define acceleration profile $\qquad b_{start} := 5550 \cdot g \qquad b_{end} := 4100 \cdot g \qquad$ Corresponding length for acceleration change: $\qquad \Delta s := 500 \cdot m$

Define the slope of the acceleration profile. Since the track length is not known a priori, it is set to sa, the track length for constant acceleration.

$$m_0 := \frac{b_{end} - b_{start}}{\Delta s} \qquad\qquad m_0 = -28.44 \, sec^{-2} \qquad\qquad acc(s) := m_0 \cdot s + b_{start}$$

$$TL := 0 \cdot m, 5 \cdot m .. \Delta s$$

Acceleration Profile
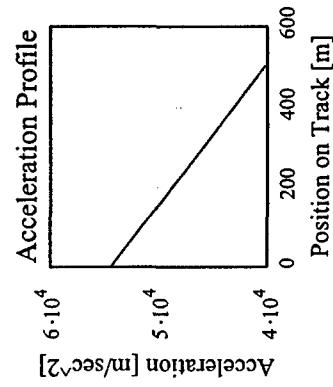
The acceleration follows a linear decrease over the distance Δs.

The differential equation describing the acceleration profile can be solved analytically for velocity and position of the sled as a function of time t. b_{start} is the acceleration at t = 0 and m_o is the slope of the acceleration profile (see above). The following solution is obtained.

$$b_{start} + m_o \cdot x = \frac{d^2}{dt^2} x(t) \cdot$$

$$\text{(Eq. 1)} \quad v(t) = \frac{b_{start}}{\sqrt{m_o}} \cdot \sinh\left(\sqrt{m_o} \cdot t\right)$$

$$\text{(Eq. 2)} \quad x(t) = \frac{b_{start}}{m_o} \cdot \left(\cosh\left(\sqrt{m_o} \cdot t\right) - 1.\right)$$

$$c_o := \sqrt{m_o}$$

Acceleration time (from Eq. 1)

$$T_{acc} := \frac{1}{c_o} \cdot asinh\left(\frac{c_o}{b_{start}} \cdot ve\right)$$

$$T_{acc} = 0.14 \, sec$$

Track length (from Eq. 2)

$$Sa := \frac{b_{start}}{m_o} \cdot \left(\cosh\left(c_o \cdot T_{acc}\right) - 1.\right)$$

$$Sa = 521.09 \, m$$

Acceleration at end of track

$$acc(Sa) = 4.04 \times 10^3 \, g$$

Acceleration Forces

	Track Start	Track End
Force to overcome track slope	$F_{slope} := M_{tot} \cdot g \cdot \sin\left(\alpha_{track}\right)$	$F_{slope} = 0.73 \, kN$
	$F_{acc}(s) := M_{tot} \cdot acc(s)$	$F_{acc}(0 \cdot m) = 5.71 \times 10^3 \, kN$	$F_{acc}(Sa) = 4.16 \times 10^3 \, kN$
Total Force (acceleration + lift)	$F_{tot}(s) := F_{slope} + F_{acc}(s)$	$F_{tot}(0 \cdot m) = 5.72 \times 10^3 \, kN$	$F_{tot}(Sa) = 4.16 \times 10^3 \, kN$
Estimate total force including magnetic drag (~5 %)	$F_{Acc}(s) := 1.05 \cdot F_{tot}(s)$	$F_{Acc}(0 \cdot m) = 6 \times 10^3 \, kN$	$F_{Acc}(Sa) = 4.37 \times 10^3 \, kN$

Aerodynamic Drag Force

$SS := 0 \cdot m, 5 \cdot m .. Sa$

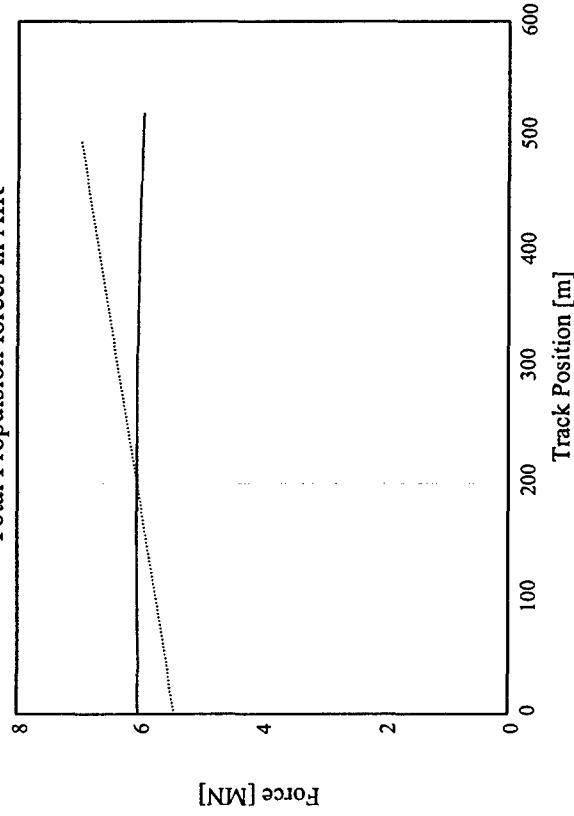$FAir(s, A, \rho, T, \gamma) :=$ | "Add air drag with drag increase and the acceleration force"

"Convert position 's' on the track to velocity"

$$t \leftarrow \frac{1}{c_o} \cdot acosh\left(s \cdot \frac{m_o}{b_{start}} + 1\right)$$

$$v \leftarrow \frac{b_{start}}{c_o} \cdot sinh(c_o \cdot t)$$

$$F_{drag}(v, A, \rho) \cdot dragIncr(v, T, \gamma) + F_{Acc}(s)$$

Total Propulsion forces in AIR

Force [MN] vs Track Position [m]

The acceleration profile has been optimized to make the required propulsion force independent of track position (solid red curve). For this case the same linear motor system is used along the track.
However, since it is most likely difficult to produce the same driving force in the linear motor at the very high speeds, it might be beneficial to use an even lower acceleration towards the end of the track.
The dashed red curve shows the required force for constant acceleration.

Determine velocity versus track position for given acceleration profile:

$$\text{vel}(s, c_o, m_o, b_{start}) := \begin{vmatrix} \text{"Determine sled velocity as a function of track position"} \\ t \leftarrow \dfrac{1}{c_o} \cdot \text{acosh}\left(s \cdot \dfrac{m_o}{b_{start}} + 1\right) \\ v \leftarrow \dfrac{b_{start}}{c_o} \cdot \sinh(c_o \cdot t) \end{vmatrix}$$

Save profile for air:

$$jt := 0 .. 100 \qquad TAir_{jt} := \dfrac{Sa}{100} \cdot jt \qquad VAir_{jt} := \text{vel}\left(TAir_{jt}, c_o, m_o, b_{start}\right)$$
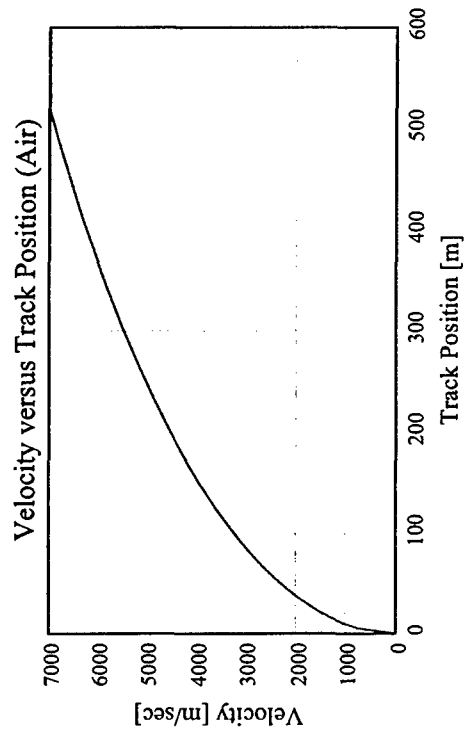
Velocity versus Track Position (Air)

Peak Power

The required power as a function of track position for the new (optimized) acceleration profiles is shown in the following diagram:

Power versus Track Position in Air
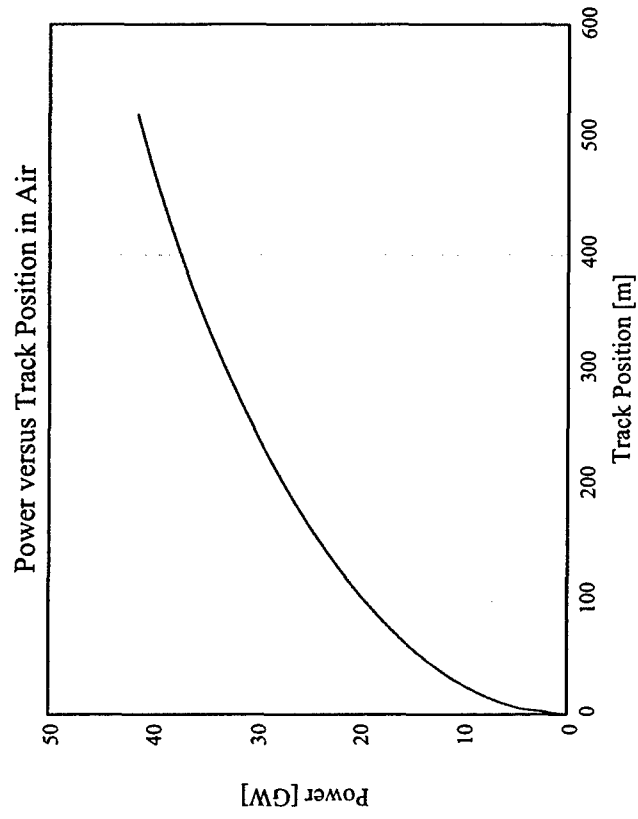
Optimization for Helium

Define acceleration profile

$$b_{start} := 5550 \cdot g \qquad b_{end} := 4100 \cdot g \qquad \text{Corresponding length for acceleration change:} \qquad \Delta s := 500 \cdot m$$

$$m_o := \frac{b_{end} - b_{start}}{\Delta s} \qquad m_o = -28.44 \, sec^{-2} \qquad acc(s) := m_o \cdot s + b_{start} \qquad c_o := \sqrt{m_o} \qquad c_o = 5.33i \, sec^{-1}$$

Acceleration time (*from Eq. 1*)

$$T_{acc} := \frac{1}{c_o} \cdot asinh\left(\frac{c_o}{b_{start}} \cdot ve\right) \qquad T_{acc} = 0.14 \, sec$$

Track length (*from Eq. 2*)

$$Sa := \frac{b_{start}}{m_o} \cdot \left(\cosh(c_o \cdot T_{acc}) - 1.\right) \qquad Sa = 521.09 \, m$$

Acceleration at end of track

$$acc(Sa) = 4.04 \times 10^3 \, g$$

Acceleration Forces

	Track Start	Track End
Force to overcome track slope $F_{slope} := M_{tot} \cdot g \cdot \sin(\alpha_{track})$	$F_{slope} = 0.73 \, kN$	
Total Force (acceleration + lift) $F_{acc}(s) := M_{tot} \cdot acc(s)$	$F_{acc}(0 \cdot m) = 5.71 \times 10^3 \, kN$	$F_{acc}(Sa) = 4.16 \times 10^3 \, kN$
$F_{tot}(s) := F_{slope} + F_{acc}(s)$	$F_{tot}(0 \cdot m) = 5.72 \times 10^3 \, kN$	$F_{tot}(Sa) = 4.16 \times 10^3 \, kN$
Estimate total force including magnetic drag (~5 %) $F_{Acc}(s) := 1.05 \cdot F_{tot}(s)$	$F_{Acc}(0 \cdot m) = 6 \times 10^3 \, kN$	$F_{Acc}(Sa) = 4.37 \times 10^3 \, kN$

15

$$\text{FHelium}(s, A, \rho, T, \gamma) := \begin{array}{l} \text{"Add air drag with drag increase and the acceleration force"} \\[4pt] \text{"Convert position 's' on the track to velocity"} \\[4pt] t \leftarrow \dfrac{1}{c_o} \cdot \text{acosh}\left(s \cdot \dfrac{m_o}{b_{start}} + 1\right) \\[12pt] v \leftarrow \dfrac{b_{start}}{c_o} \cdot \sinh(c_o \cdot t) \\[10pt] F_{drag}(v, A, \rho) \cdot \text{dragIncr}(v, T, \gamma) + F_{Acc}(s) \end{array}$$

$SS := 0 \cdot m, 5 \cdot m .. Sa$

Total Propulsion forces in Helium

The diagram shows the required force (blue solid curve) for helium with the same acceleration profile as for air. Since the drag in the helium atmosphere is smaller than in air, the required force falls off towards the end of the track.
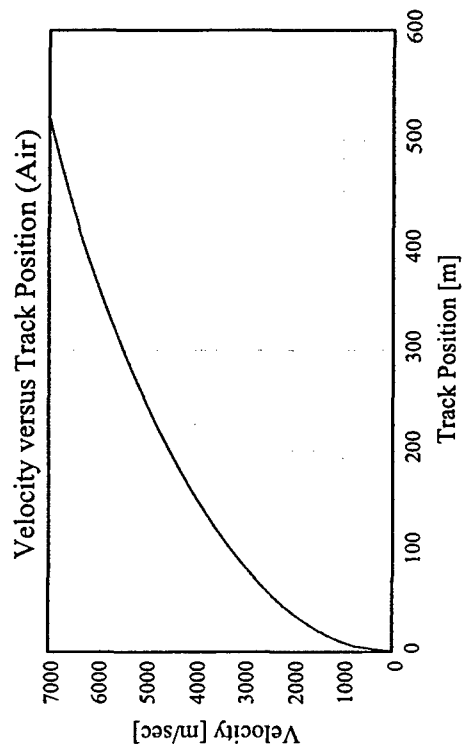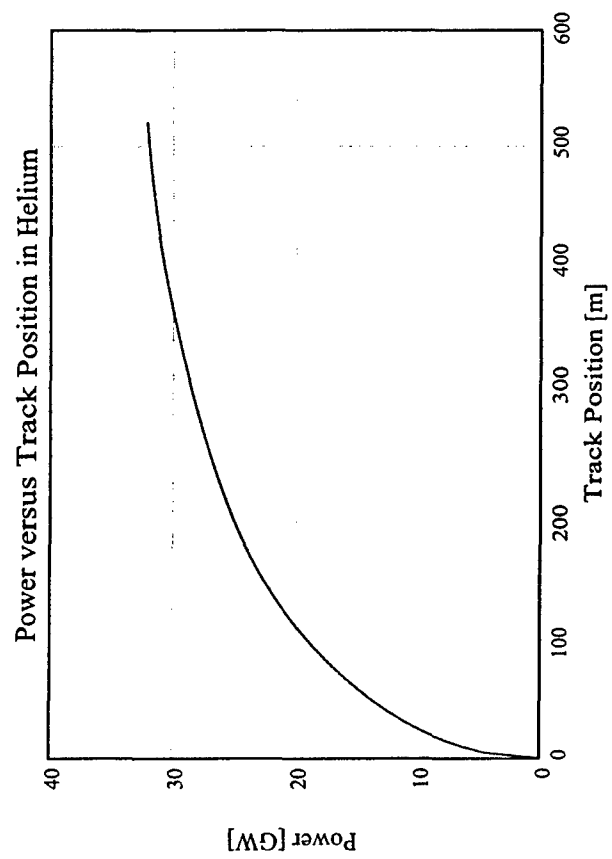The reduced force requirements towards the track end should help the linear motor design.

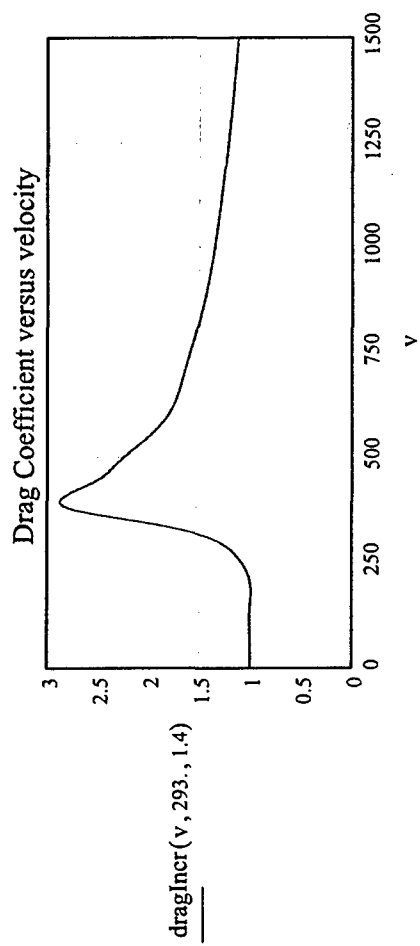The dashed blue curve shows the required force for constant acceleration.

Peak Power

The required power as a function of track position for the new (optimized) acceleration profiles is shown in the following diagram:

$$THelium_{jt} := \frac{Sa}{100} \cdot jt \qquad VHelium_{jt} := vel\left(THelium_{jt}, c_o, m_o, b_{start}\right)$$

Velocity versus Track Position (Air)

Power versus Track Position in Helium

Track Position [m]

Power [GW]

Drag Coefficient versus velocity

dragIncr(v , 293. , 1.4)

v

General definitions:

$\text{Mach}_{air} \equiv 344 \cdot \dfrac{m}{sec}$ $\text{Mach}_{helium} \equiv 1000 \cdot \dfrac{m}{sec}$

$\text{Mwatt} \equiv 10^6 \cdot \text{watt}$

$\text{Gwatt} \equiv 10^9 \cdot \text{watt}$

$\text{Mjoule} \equiv 10^6 \cdot \text{joule}$

$\text{Gjoule} \equiv 10^9 \cdot \text{joule}$

$\text{kN} \equiv 10^3 \cdot \text{newton}$

$\text{MN} \equiv 10^6 \cdot \text{newton}$

$\text{dollar} \equiv 1$

$\text{Cost\_kW\_hour} \equiv 0.05 \cdot \dfrac{\text{dollar}}{\text{kW} \cdot \text{hr}}$

Drag coefficient versus Mach number

$$M_{num} \equiv \begin{pmatrix} 0.0 \\ 0.2 \\ 0.4 \\ 0.6 \\ 0.8 \\ 0.9 \\ 1.0 \\ 1.1 \\ 1.2 \\ 1.3 \\ 1.4 \\ 1.6 \\ 1.8 \\ 2.0 \\ 2.5 \\ 3.0 \\ 4.0 \\ 5.0 \\ 6.0 \end{pmatrix} \qquad Drag \equiv \begin{pmatrix} 0.15 \\ 0.15 \\ 0.15 \\ 0.15 \\ 0.175 \\ 0.21 \\ 0.3 \\ 0.415 \\ 0.42 \\ 0.375 \\ 0.35 \\ 0.30 \\ 0.265 \\ 0.25 \\ 0.22 \\ 0.20 \\ 0.175 \\ 0.158 \\ 0.15 \end{pmatrix}$$

Spline fit and interpolation:

$$vs := cspline\left(M_{num}, Drag\right)$$

$$ddrag(m) := if\left(m < 6, interp\left(vs, M_{num}, Drag, m\right), 0.15\right)$$

The published data shown in the table above are for a drag coefficient of 0.15. We assume that the same functional dependence of drag coefficient versus Mach number can be used for other values of the drag coefficient. Under these assumptions the velocity dependence of any drag coefficient can be estimated by multiplying the coefficient with the function dragIncr(v, T, γ). The argument v is the velocity in m/sec, T is absolute temperature in K and γ is the heat capacity ratio Cp/Cv ~ 1.4 (air) and 1.67 (helium). R = 287 J/kg/K is the ideal gas constant.

$$\text{dragIncr}(v, T, \gamma) := \begin{vmatrix} \text{RR} \leftarrow 287 \\ \text{N}_{\text{mach}} \leftarrow \dfrac{v}{\sqrt{\gamma \cdot \text{RR} \cdot T}} \\ \text{if}\left(\text{N}_{\text{mach}} < 6, \dfrac{\text{interp}(vs, M_{\text{num}}, \text{Drag}, N_{\text{mach}})}{.15}, 1\right) \end{vmatrix}$$

Drag Coefficient versus velocity

dragIncr(v, 293., 1.4)

v